JOURNAL OF AIRCRAFT
Vol. 47, No. 4, July–August 2010

Prediction and Analysis of Main Rotor Loads in a Prescribed Pull-Up Maneuver

A. Abhishek*
University of Maryland, College Park, Maryland 20742
Anubhav Datta†
ELORET Corporation, Moffett Field, California 94035
and
Shreyas Ananthan‡ and Inderjit Chopra§
University of Maryland, College Park, Maryland 20742

DOI: 10.2514/1.46899

This paper predicts and analyzes main rotor airloads, structural loads, and swashplate servo loads in a prescribed high-*g* pull-up maneuver. A multibody finite-element structural model is coupled with a transient lifting-line aerodynamic model. The structural model includes a swashplate model to calculate servo loads. The lifting-line model combines airfoil tables, a Weissinger–L near-wake time-marching free wake, and a semiempirical dynamic stall model. The maneuver data were taken from the Army/NASA UH-60A Airloads Program Flight Counter 11029. The primary objective of this paper is to isolate the effects of structural dynamics, free wake, dynamic stall, and pitch control angles in order to determine the key loads mechanisms in this flight. The structural loads are first calculated using airloads measured in flight. The measured airloads are then replaced with a lifting-line coupled analysis, which is ideally suited to isolate the effects of free wake and dynamic stall. It is concluded that the maneuver is almost entirely dominated by stall, with little or no wake-induced effect on blade loads, even though the wake cuts through the disk twice during the maneuver. At the peak of the maneuver, almost 75% of the operating envelope of a typical airfoil lies beyond stall. The mechanism of dynamic stall, in the analysis, consists of multiple cycles within a wide disk area. The peak-to-peak structural loads prediction from the lifting-line analysis shows an underprediction of 10–20% in flap and chord bending moments and 50% in torsion loads. The errors stem from the prediction of four- and five-revolution stall loads. Swashplate dynamics appear to have a significant impact on the servo loads (unlike in level flight), with a more than 50% variation in peak loads.

Introduction

THE main rotor structural loads encountered during unsteady maneuvers are important to size different critical components of the rotor system, particularly for advanced combat helicopters. These include the blade structural loads, the control/pitch-link loads, and the swashplate servo loads. Accurate and consistent prediction of the maneuver loads is necessary to reduce the risks and costs associated with the use of previously obtained flight-test data as a basis for design. This paper predicts and analyzes helicopter main rotor loads during a prescribed pull-up maneuver. The blade airloads, the structural loads, the pitch-link loads, and the swashplate servo loads are calculated using a multibody structural dynamics model coupled with a free-wake-based unsteady lifting-line aerodynamic model, and they are validated with UH-60A flight-test data.

The state-of-the-art prediction of the main rotor loads in steady level flight (critical for vibratory loads), using computational fluid dynamics (CFD) and computational structural dynamics (CSD) coupled analysis, can be found in [1]. Loads prediction in unsteady maneuvers, critical for peak design loads, has remained a challenging task. First, all three of the important aerodynamic mechanisms of rotor wake intertwining, transonic pitching moments, and dynamic stall can occur simultaneously in a maneuver. Second, an inverse solution procedure to determine the trim variables (pitch control angles, vehicle attitude angles, and yaw control) in order to fly a prescribed trajectory is quite involved and not yet available. In steady level flight, the trajectory is simple, and the aircraft Euler equations reduce to six equilibrium equations from which the trim variables are easily determined. The complexity of the solution procedure has been the primary hurdle for a first principle prediction of maneuver loads. Today, extensive flight-test data from the U.S. Army/NASA Airloads Program (see [2,3]) have opened the opportunity to bypass this complexity. The measured values of rotor controls, aircraft attitudes, and flight trajectory can now all be prescribed from flight-test data in order to focus solely on the load mechanisms.

The maneuvers with highest loads of the UH-60A helicopter has been studied in great detail by Bousman [4] and Kufeld [5]. Based on the criteria of six structural measurements, which includes pitch-link load, torsion moment (30%R), and flap and chord bending moments (11.3 and 60%R), they identified and ranked the severest maneuvers. Out of the two severest maneuvers, the second most severe maneuver, designated by Counter 11029, is studied in this paper. Note that at this time the test data are made available only for this maneuver. This maneuver is based on the Utility Tactical Transport Aerial System (UTTAS) maneuver of the original UH-60A design specification. It is a dynamic pull up that reaches 2.12 g at 139 kt and produces the highest root flap bending moment and the third-highest oscillatory pitch-link load of all the UH-60A maneuvers. The measured load factor and velocity ratio are shown in Figs. 1 and 2. Even though the pitch-link load is only third highest of all the maneuvers, it still exceeds the loads encountered in operational use. For example, the peak-to-peak pitch-link loads at this flight are 20% higher than those encountered during free engagement air-to-air combat test flights of similar kind [6]. The aircraft attitude angles and angular rates are shown in Figs. 3a and 3b. The aircraft pitch angle when reduced using the measured flight-path angle (not shown) and a

Presented as Paper 2009-2466 at the 50th AIAA/ASME/ASCE/AHS/ASC Structures, Structural Dynamics, and Materials Conference, Palm Springs, CA, 4–7 May 2009; received 27 August 2009; accepted for publication 13 December 2009.

*Graduate Research Assistant, Department of Aerospace Engineering.
†Rotorcraft Dynamicist, NASA Ames Research Center.
‡Assistant Research Scientist, Department of Aerospace Engineering.
§Department of Aerospace Engineering; Alfred Gessow Professor and Director, Alfred Gessow Rotorcraft Center. Fellow AIAA.

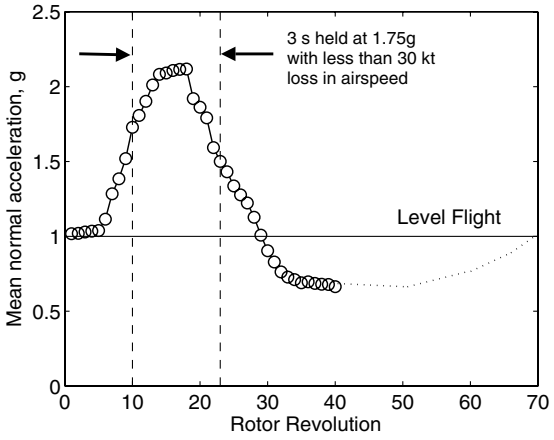

Fig. 1 Measured mean load factor.

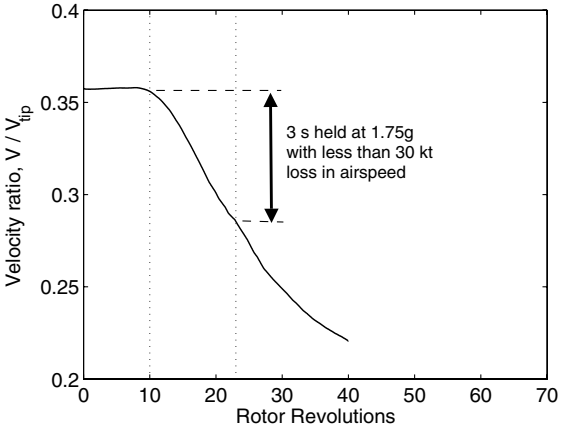

Fig. 2 Measured aircraft velocity ratio.

3 deg forward built-in shaft angle produces the effective shaft tilt with respect to the oncoming flow (see Fig. 4). The wake is expected to pass through the rotor disk around revolutions 10 and 24: first from below to above and then from above to below.

A high-fidelity simulation of the prescribed UTTAS pull up was carried out by Bhagwat et al. [7,8] using a multibody finite element structural model coupled with a Reynolds-averaged Navier–Stokes (RANS) model. This work demonstrated RANS capability in predicting two rotor dynamic stall cycles for the first time for a maneuver and showed that the oscillatory blade structural loads could be predicted with increased accuracy using an isolated rotor calculation. Abhishek et al. [9] carried out a simpler lifting-line analysis, also for an isolated rotor, with an attempt to calculate the

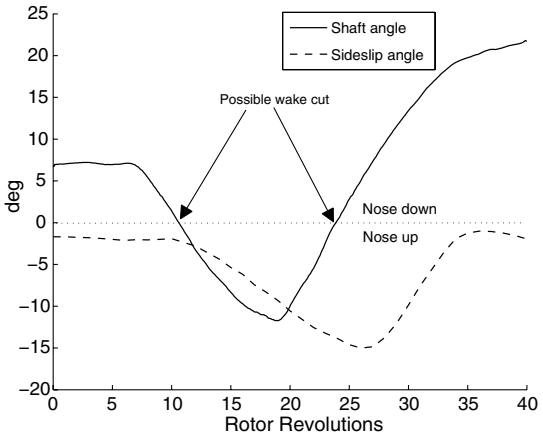

Fig. 4 Aircraft shaft angle with respect to oncoming flow and sideslip angle.

rotor pitch control angles: it was unsuccessful due to large errors stemming from the unknown horizontal tail lift during the maneuver and an inability to predict the maneuver trajectories in absence of detailed aircraft data. Subsequently, with availability of flight-test control angles, several researchers have predicted loads for this prescribed maneuver: Abhishek et al. [10] and Yeo [11] focused on lower-fidelity lifting-line predictions, [7,8] compared the lifting-line model's capabilities with CFD/CSD analysis, [12] employed wake-coupling CFD/CSD approach, and [13] examined the effect of time-accurate coupling using RANS. The lifting-line analyses in general shows less satisfactory correlation with measured flight-test data when compared with CFD analysis. The present paper uses lifting-line aerodynamics with the objective of isolating the stall and wake effects.

The objectives of this paper are 1) to isolate the effects of structural dynamics, free-wake inflow, dynamic stall, and rotor pitch control angles, separately, on the prediction of maneuver loads and 2) to examine the prediction accuracy of airloads, blade loads, and swashplate servo loads using an unsteady lifting-line aerodynamic model. The accuracy of the structural model by itself is studied first, in isolation, using airloads measured in flight. The multibody finite element model is then coupled with a transient lifting-line aerodynamic model to study the impact of free wake, dynamic stall, and control pitch angles on predicted airloads, blade loads, pitch-link loads, and swashplate servo loads.

Analysis Methodologies

Rotor–Swashplate Structural Model

The rotor model consists of the flexible blades, rigid root end control components, and a swashplate model. Each blade is modeled as a fully articulated beam with flap and lag hinges coincident at

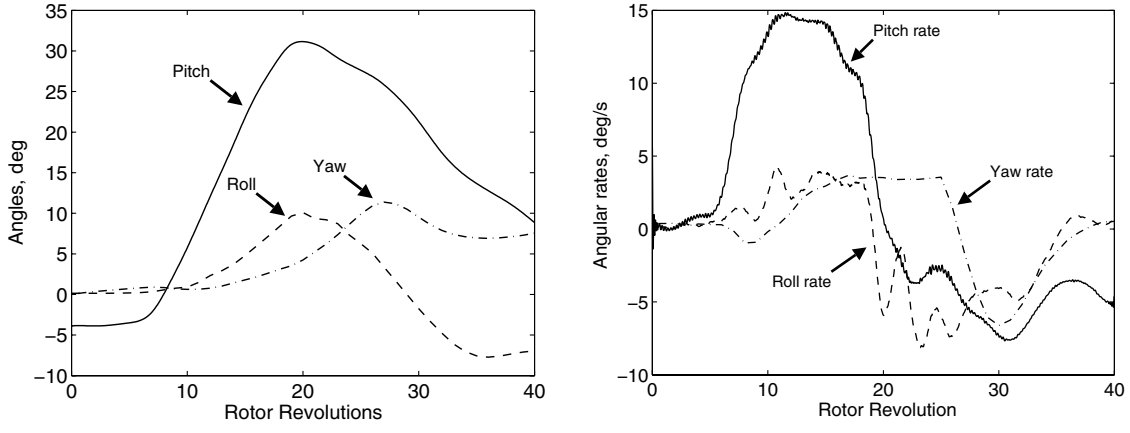

Fig. 3 Measured aircraft attitude and rates.

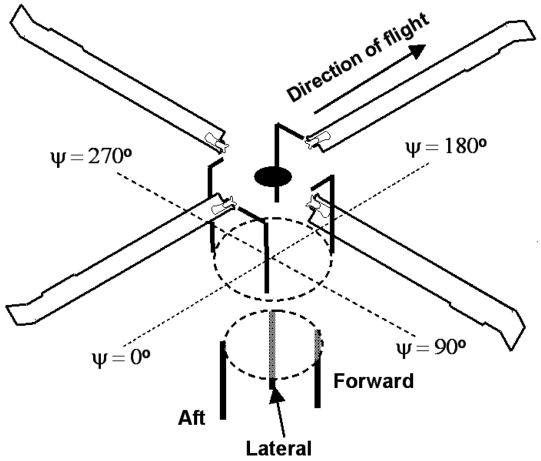

Fig. 5 Schematic of UH-60A blade–swashplate model.

4.66% span. It is discretized using 20 nonlinear beam elements, with each element having a local frame of reference attached to it in order to model arbitrary large deformations [14]. The blade property data are obtained from the NASA Ames master database. The swept portion of the blade is modeled using three elements with swept elastic axis. The pitch horn and the hub is modeled using rigid bodies, and the pitch link is modeled as a linear spring–damper element. The pitch-link stiffness is obtained using the measured equivalent root torsion spring stiffness of 1090 ft · lb/ deg [15].

The swashplate is modeled as a thin disk with three degrees of freedom: vertical heave, pitch up, and roll left. It is attached to the four pitch links on the top and three servo actuators at the bottom (see Fig. 5). The rotating and the nonrotating swashplates are idealized together as a single functional element, which 1) transfer loads between the servos at the bottom and the pitch links on the top, 2) transfer displacements from servos at the bottom to the pitch links at the top, and 3) applies rotating-frame to fixed-frame transformation from top to bottom. The pitch links and the servos are modeled as linear spring–damper systems. A swashplate mass of 75 kg (165 lb) is considered based on [14]. The details of the structural model and determination of swashplate and servo properties can be found therein.

Lifting-Line Aerodynamic Model

A multibladed transient lifting-line aerodynamic model is developed in this study. It incorporates two-dimensional airfoil property tables, a Weissinger–L near-wake model, free wake, and the Leishman–Beddoes dynamic stall model [16] for attached and separated flows.

The core of the analysis is the Leishman–Beddoes [16] dynamic stall model, which acts on the effective section angles of attack after including free-wake and near-wake effects. At each azimuth (i.e., time), the inputs into the lifting-line model are the blade

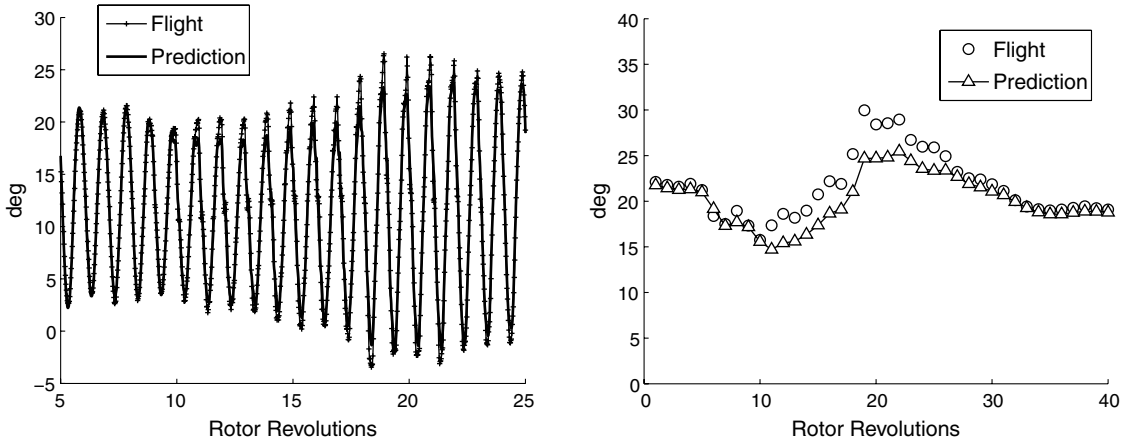

Fig. 6 Measured (blade 3) and predicted pitch angle at root: a) time history and b) peak-to-peak. (Predictions made using flight-test airloads. Time history shown for only 20 revolutions for clarity.)

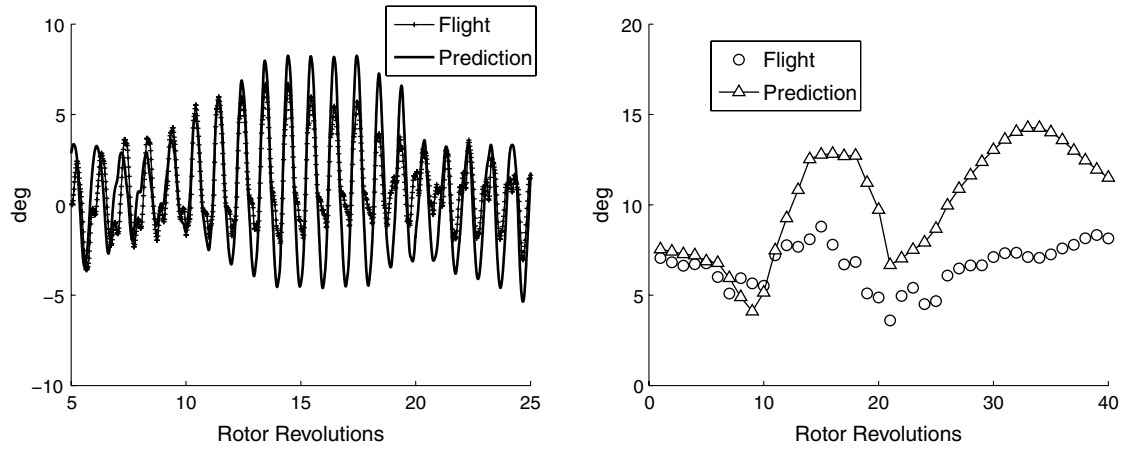

Fig. 7 Measured (blade 1) and predicted flap angle at root: a) time history and b) peak-to-peak. (Predictions made using flight-test airloads. Time history shown for only 20 revolutions for clarity.)

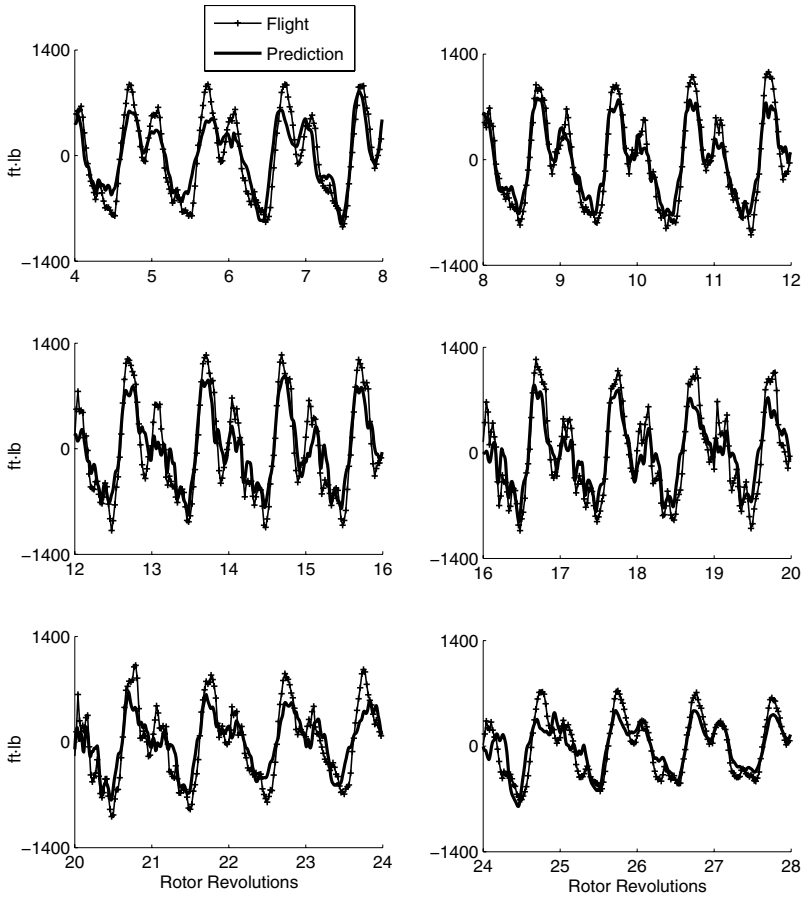

Fig. 8 Measured and predicted flap bending moment at 50%*R*. (Predictions made using flight-test airloads, and mean removed.)

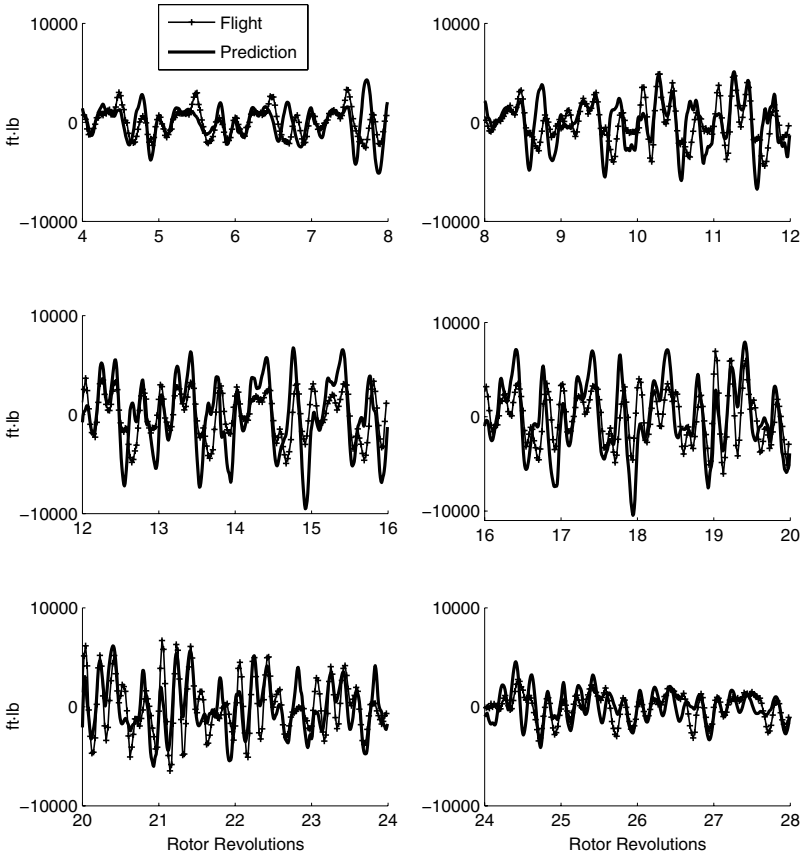

Fig. 9 Measured and predicted lag bending moment at 50%*R*. (Predictions made using flight-test airloads, and mean removed.)

deformations for all blades, the instantaneous advance ratio, the shaft tilt angle, the rotor pitch, the roll angles, the angular rates, and the control angles. The outputs from the model are the airloads on all of the blades and the inflow velocities at the blade control points (swept three-quarter-chord line). Within the model, the current blade deformations are used along with the inflow velocities, stored from the previous time step, to calculate the airloads, the bound circulation distribution, the near-wake trailer strengths, and the near-wake induced velocities at the blade control points. The near-wake induced velocities are then used to recalculate the airloads. The bound circulation distribution and the current blade deformations are then used to advance the free-wake solution to the current time step. This free-wake solution is used in the calculation of airloads in the next time step. The free wake is the same as the Ananthan–Leishman [17] model, modified to incorporate flexible blade deformations in flap, lag, and torsion, and the bound circulation strengths as calculated previously. The wake models account for only trailed vorticity; the effect of shed vorticity is incorporated using the Leishman–Beddoes unsteady aerodynamic model. At each time step, the unsteady model is updated based on the change in airloads from the previous time step. The transient aerodynamic analysis has been validated in [9] for level-flight conditions.

Transient Solution Procedures

The solution procedure for the analysis with measured airloads, damper loads, and control angles starts with a periodic solution for the first revolution, which corresponds to the steady flight condition. The steady periodic solution is obtained by using the periodic airloads taken from revolution 1 of the maneuver by letting the analysis run for 40 revolutions. Once the dynamic response settles into periodicity, then the maneuver is initiated. Note that, unlike in level flight, it is not possible to iteratively correct the root pitch control angles based on the calculated pitch-link deflection. However, this error (as shown later) is insignificant. The main source of error is the absence of airloads data (gauge out) at the 55%R station.

The solution procedure for the coupled multibody/lifting-line analysis requires that the measured control angles be corrected based on initial trim conditions. The level flight at the beginning of the maneuver must be simulated using calculated rotor control angles (and not the flight-test measured values) for reasons given in the Introduction. These are calculated using a moment trim, targeting thrust, and hub moments of 17,300 lb, 6059 ft · lb roll left, and 4182 ft · lb pitch down, respectively, corresponding to the high-speed level-flight counter 8534.

The maneuver is initiated from the level-flight condition by smoothly merging the control angles, as per the incremental procedure outlines in the section on Analysis Methodologies. The velocity ratio, the shaft angles, the attitudes, and the rates are subsequently prescribed using the test conditions. During the maneuver, the structural dynamic and the aerodynamic models are advanced in time, as per the solution procedure outlined earlier. The procedure is the same as a CFD/CSD tight coupling (rotorcraft terminology), except that, instead of CFD, a lifting-line model is being used. No subiterations are employed to ensure strict time accuracy (i.e., deflections at a given azimuth are calculated based on airloads from the previous azimuth). The calculated deflections are then used to advance the airloads to the current azimuth. The deflections, however, are not updated based on current azimuth airloads. Note that this procedure is also referred to as loose coupling by the fixed-wing CFD/CSD researchers [18].

Prediction Using Measured Airloads

The measured airloads problem (also termed as the mechanical airloads problem) allows one to assess the accuracy of the structural model separately from the airloads model, as the time-varying measured airloads are no longer contaminated with the errors

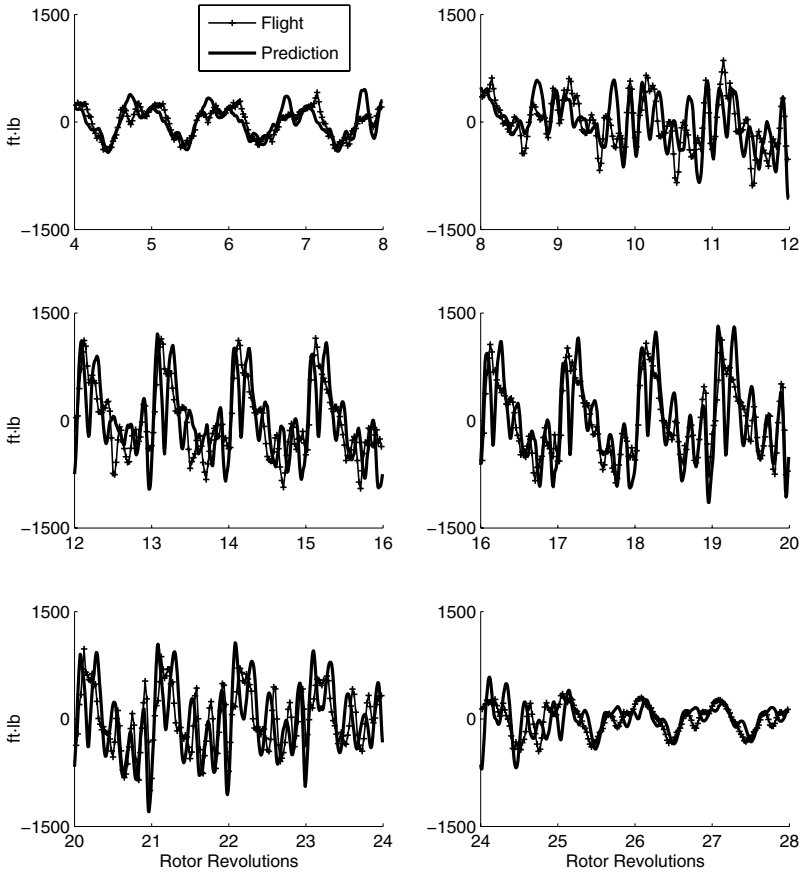

Fig. 10 Measured and predicted torsion moment at 30%R. (Predictions made using flight-test airloads, and mean removed.)

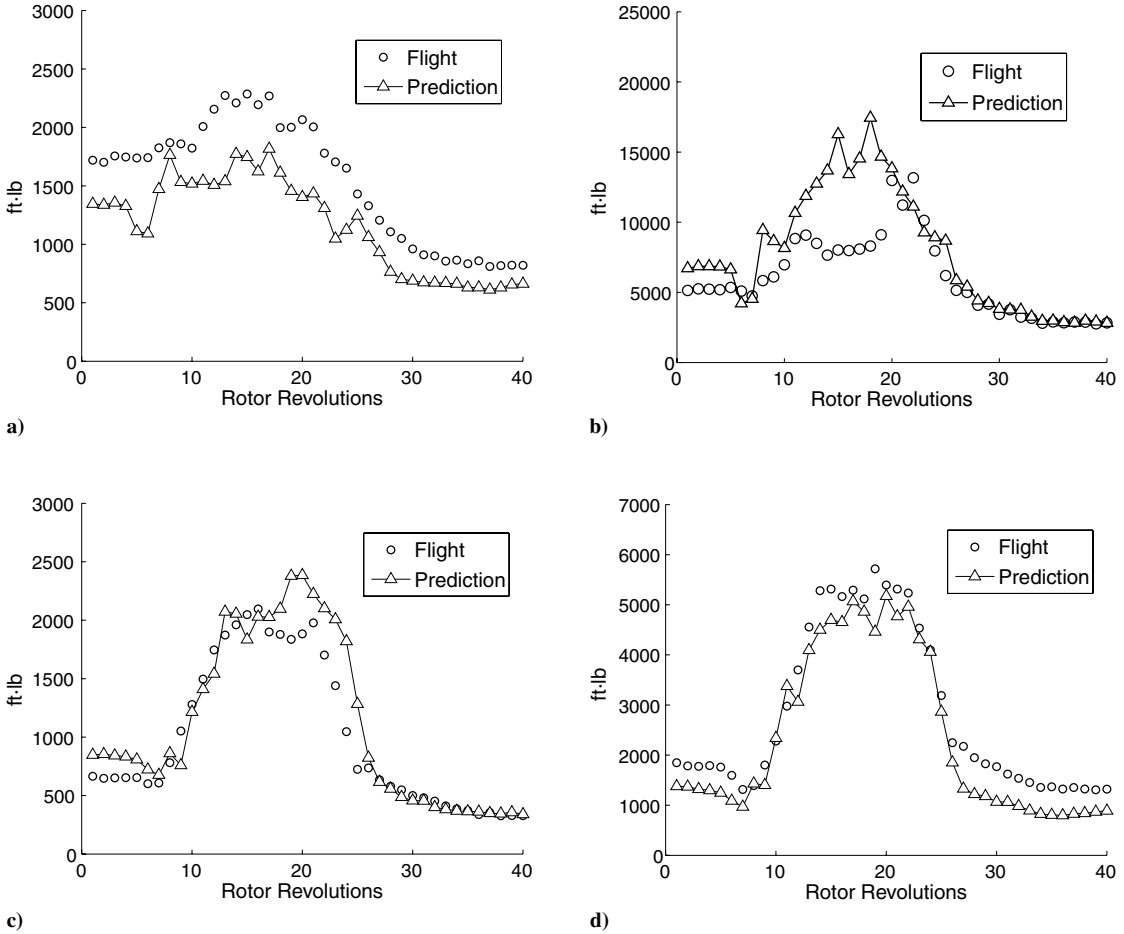

Fig. 11 Measured and predicted peak-to-peak structural loads for a) flap bending moment at 50%R, b) lag bending moment at 50%R, c) torsion moment at 30%R, and pitch-load link. (Predictions made using flight-test airloads.)

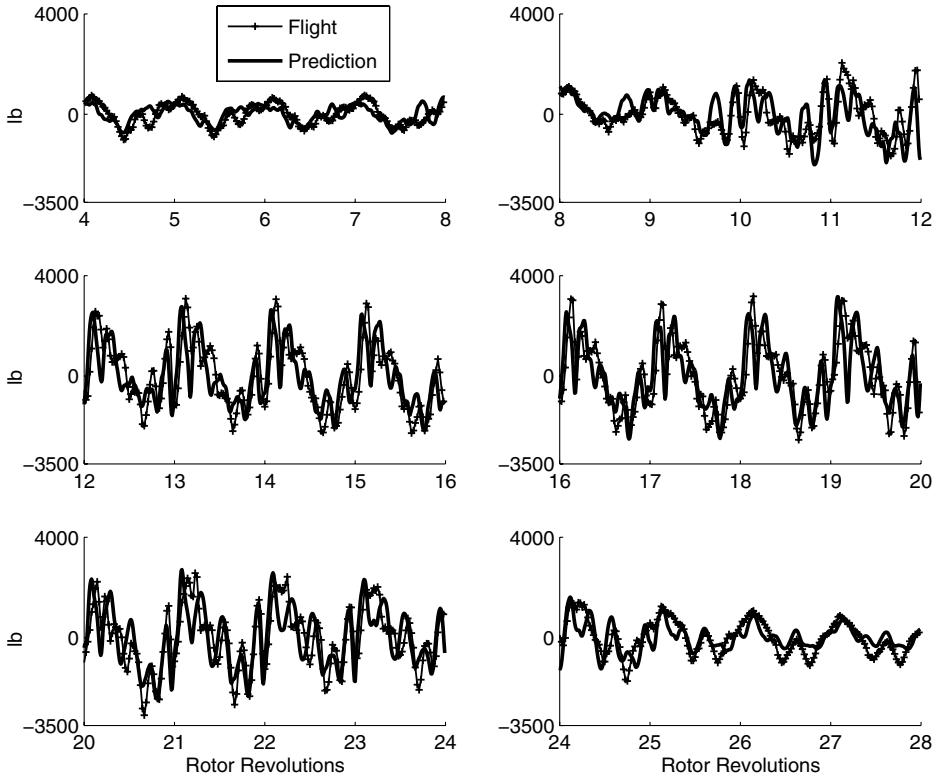

Fig. 12 Measured and predicted pitch-link load. (Predictions made using flight-test airloads and mean removed.)

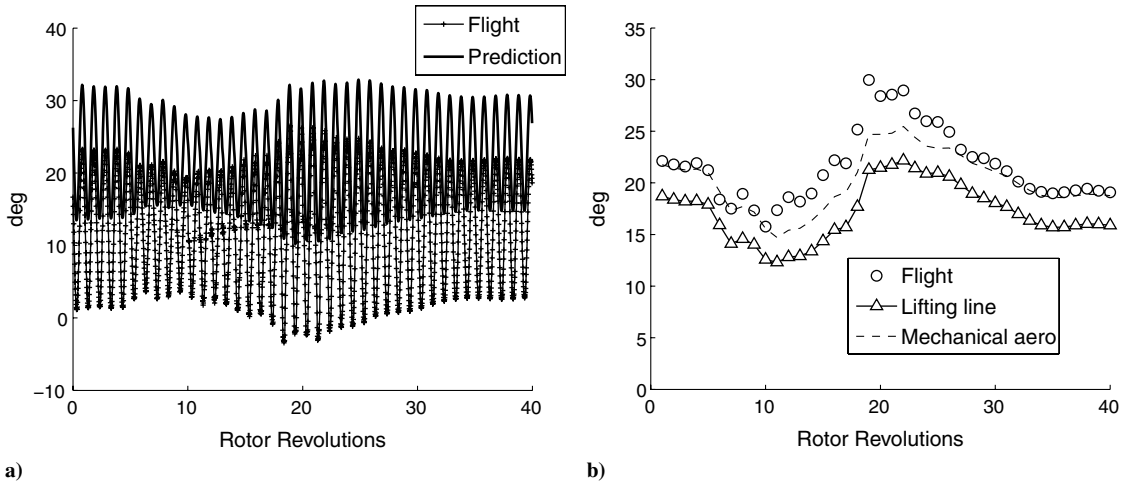

a) b)

Fig. 13 Measured (blade 3) and predicted pitch angle at root: a) time history and b) peak-to-peak. (Predictions made using dynamic stall model.)

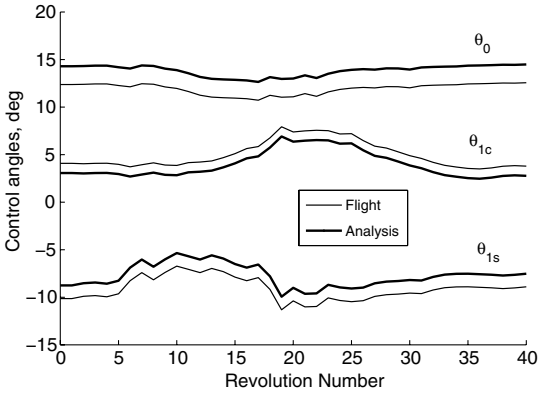

Fig. 14 Prescribed control angles for airloads flight 11029. (Angles adjusted to match initial trim.)

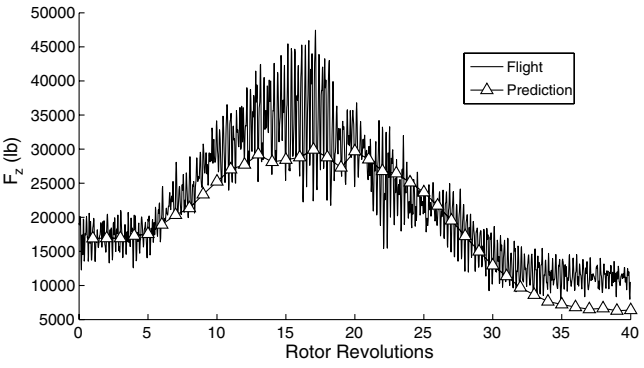

Fig. 16 Measured and predicted vertical hub force using dynamic stall model. (Flight data obtained from a measured load factor.)

associated with the predicted airloads. However, the airloads do not change with the structural response, resulting in zero aerodynamic damping. This poses a significant difficulty in obtaining a periodic solution in level flight with little structural damping, as the rotor frequencies (particularly, one revolution flapping) lie close to the rotor harmonics. Therefore, an additional damping (0.02% of critical) has to be used during the course of the analysis. This also necessitates 40 revolutions of maneuver initiation, run before the imposition of transient airloads.

Blade Root Deflections

The predicted blade pitch angle is compared with the measured values at the root (blade 3) in Fig. 6. Root pitch angle is the net result of applied rotor pitch control and elastic pitch-link deflection. The latter being small, the two sets are expected to match closely.

Figure 7 shows the predicted and measured flap angle (blade 1). Investigation of the time history reveals that, for the initial part of the maneuver (revolution numbers 0–6), the blade flap angle is predominantly one revolution, with significant two revolutions only

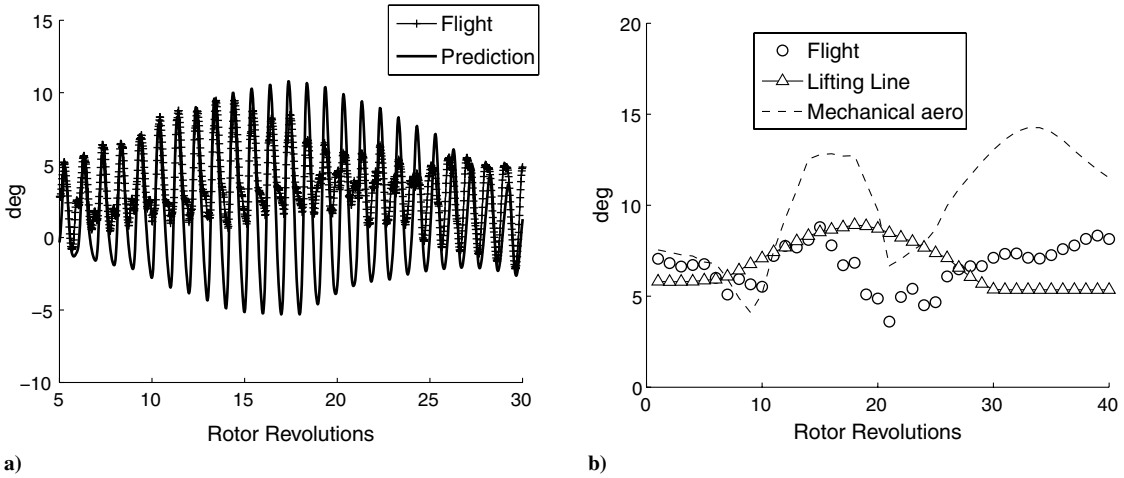

a) b)

Fig. 15 Measured (blade 1) and predicted flap angle at root: a) time history and b) peak-to-peak. (Predictions made using dynamics stall model, and time history shown for only 25 revolutions for clarity.)

in the later part of the maneuver. The analysis showed good prediction of root flap angle at the beginning of the maneuver. The flap angle is overpredicted from revolution 12 onward.

Flap and Lag Bending Loads

The predicted flap bending moments (mean removed) at 50%R are shown in Fig. 8. It is important to note that the sectional airloads at 55% radial station are not available because of failed instrumentation [4]. Therefore, the airloads have to be linearly interpolated between 40 to 67.5% radial stations. This lack of information seems to have impacted the peak-to-peak magnitude of structural loads in general (and the flap bending moment in particular) throughout the maneuver, resulting in underprediction.

Figure 9 shows the predicted lag bending moment at 50%R. The sharp gradient in the moment waveform at all blade locations and all revolutions near 180–250 deg azimuths is a direct effect of the damper force [19]. Predictions show only fair correlation with the test data at 50% radial station, particularly revolution 12 onward.

Torsion Loads

The torsion moment at 30%R is shown in Fig. 10. At the beginning of the maneuver, it is overpredicted, and there is a discrepancy in the waveform on the retreating side. This discrepancy is less pronounced in the latter part of the maneuver due to a significant natural response between four and five revolutions (the first torsion frequency is 4.4 revolutions), and the predicted magnitude shows good correlation with the test data (see Fig. 11c). The effect of stall is clearly visible. The peak-to-peak structural loads are summarized in Fig. 11. The pitch-link load (see Fig. 12) shows a similar trend.

A time-step-size sensitivity analysis is carried out to determine the convergence of blade loads with the time step, which is based on a time step of 2 deg that is used for the present analysis with mechanical airloads. A similar trend is observed for the lifting-line analysis, for which again a time step of 2 deg is used for both the time response analysis as well as the wake discretization.

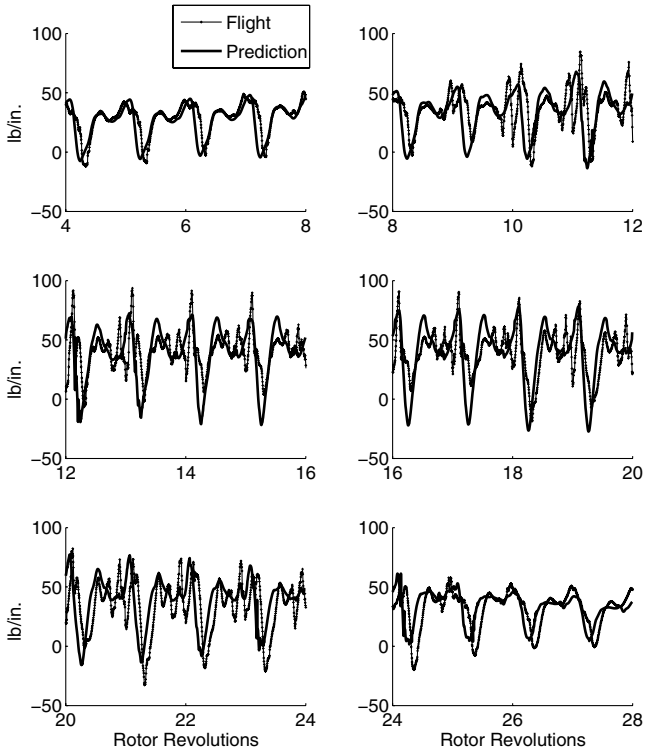

Fig. 17 Measured and predicted normal force at 86.5%R. (Predictions made using dynamic stall model.)

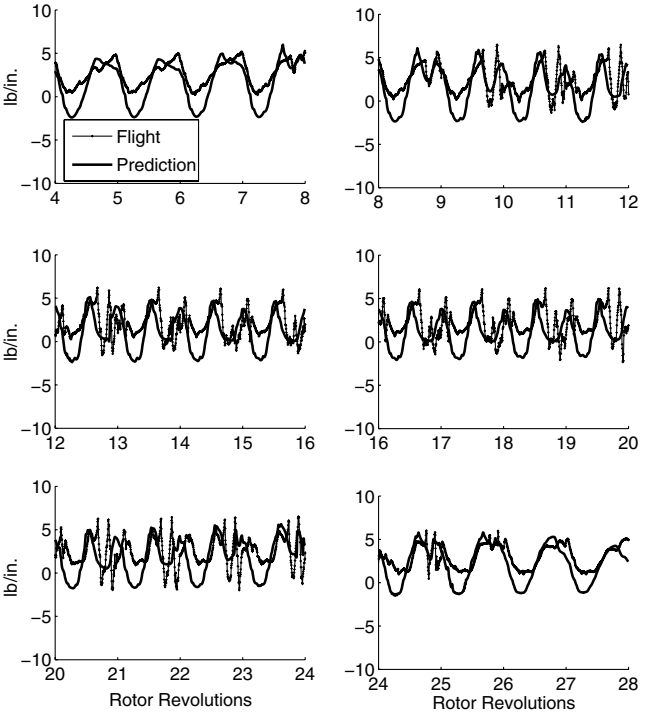

Fig. 18 Measured and predicted chord force at 86.5%R. (Predictions made using dynamic stall model.)

Prediction Using Lifting-Line Coupled Analysis

In this section, the multibody rotor structural model is tightly coupled with the transient lifting-line aerodynamic model to predict airloads, blade loads, pitch-link loads, and swashplate servo loads. The baseline results use the full-up aerodynamic model, including free wake and dynamic stall.

Blade Root Deflections

The predicted blade pitch angle is compared with the measured values in Fig. 13. There is a difference between the two, because the

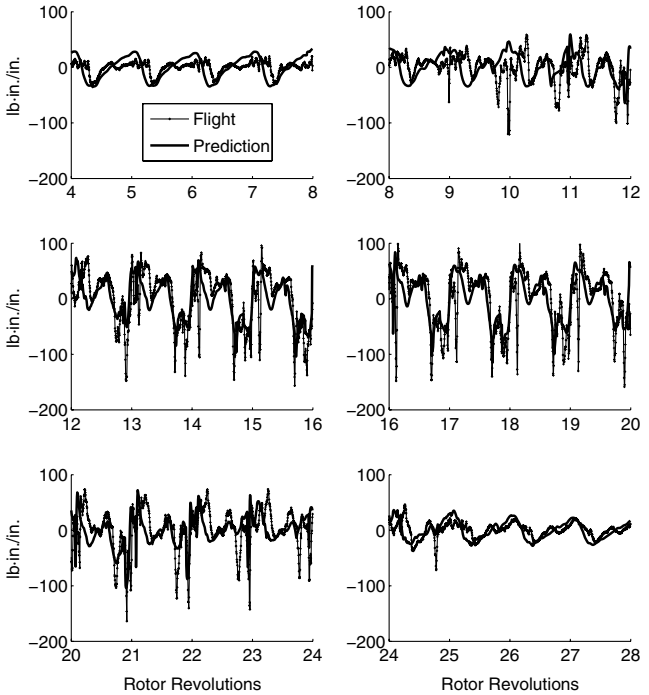

Fig. 19 Measured and predicted pitching moment at 77.5%R. (Predictions made using dynamic stall model, and mean removed.)

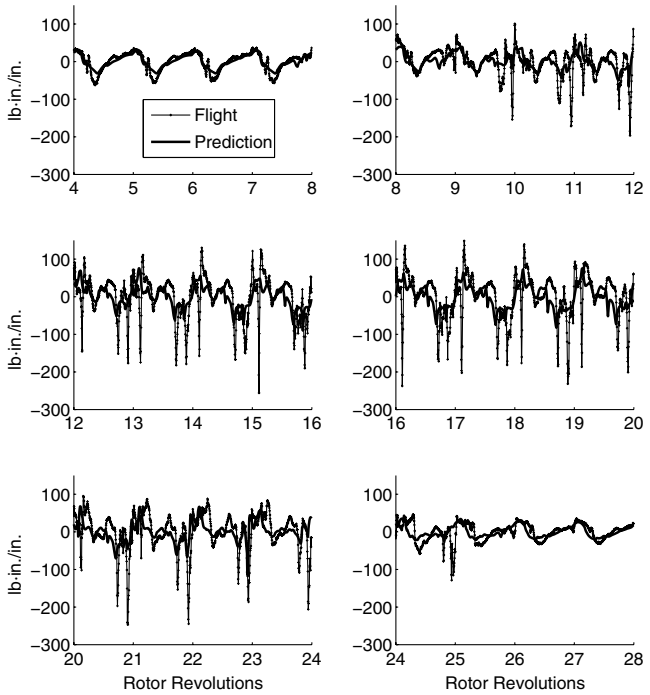

Fig. 20 Measured and predicted pitching moment at 86.5%R. (Predictions made using dynamic stall model, and mean removed.)

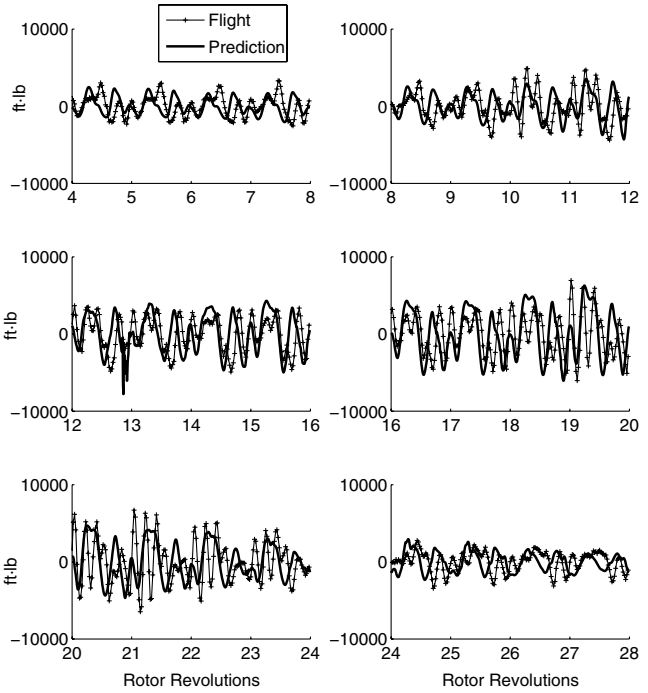

Fig. 22 Measured and predicted chord bending moment at 50%R. (Predictions made using dynamic stall model, and mean removed.)

control angle correction is applied at the beginning of the analysis in order to begin from a trimmed level-flight condition (see Fig. 14). Figure 15 shows the predicted flap angles. Unlike the mechanical airloads case, here, predictions are quite different from test data. The same trend is observed in CFD/CSD analysis as well [8,11].

Blade Airloads

The rotor hub force was not directly measured during the UH-60A Airloads Program and, hence, has to be computed indirectly by using either the load factor measurements or by integrating the sectional normal force. The load factor data are multiplied with the vehicle weight to obtain the vertical hub force for the present analysis. The predicted hub force is shown in Fig. 16. The predicted vertical hub force shows fair agreement with the flight-test data at the beginning of the maneuver when the load factor is one. As the load factor begins to increase when the helicopter starts to pull up, there is a significant difference between the prediction and the flight-test measurement (around 6000 lb). This may be due to the contributions from the fuselage and the horizontal tail, and it has been clarified by Bhagwat et al. [7].

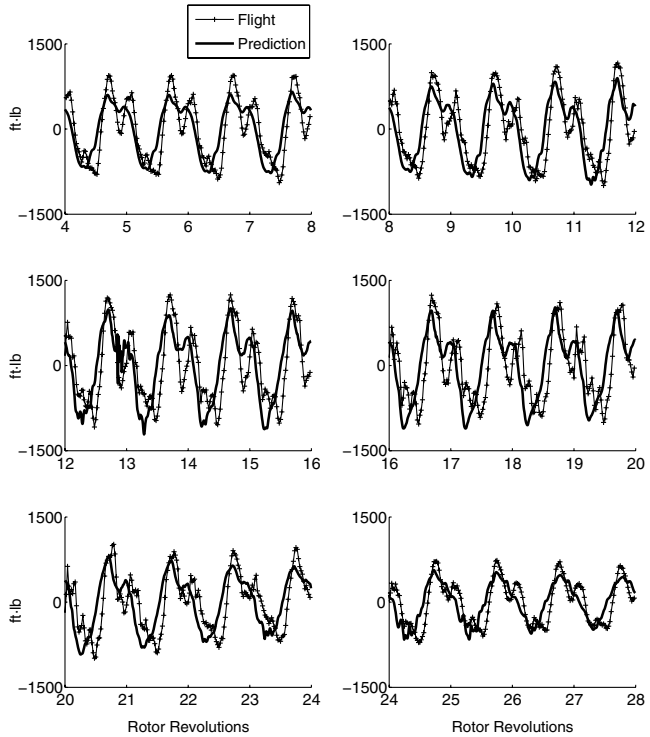

Fig. 21 Measured and predicted flap bending moment at 50%R. (Predictions made using dynamic stall model, and mean removed.)

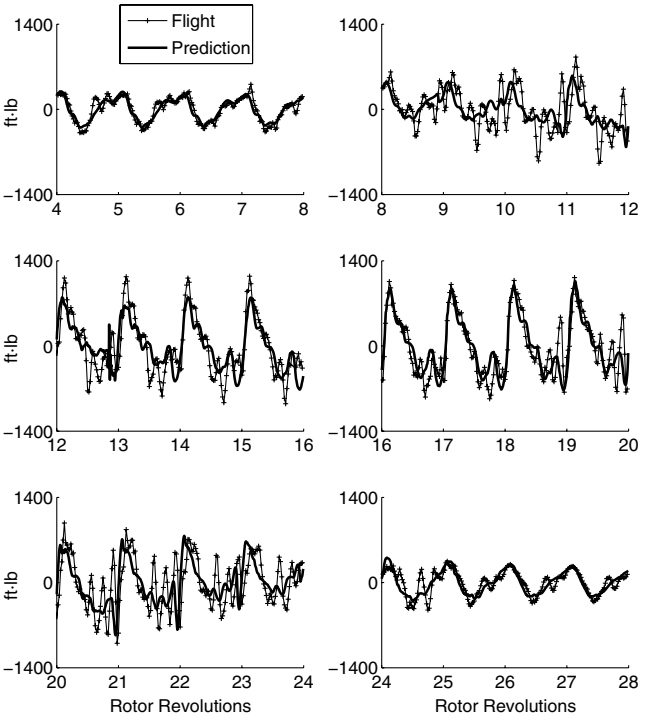

Fig. 23 Measured and predicted torsion moment at 30%R. (Predictions made using dynamic stall model, and mean removed.)

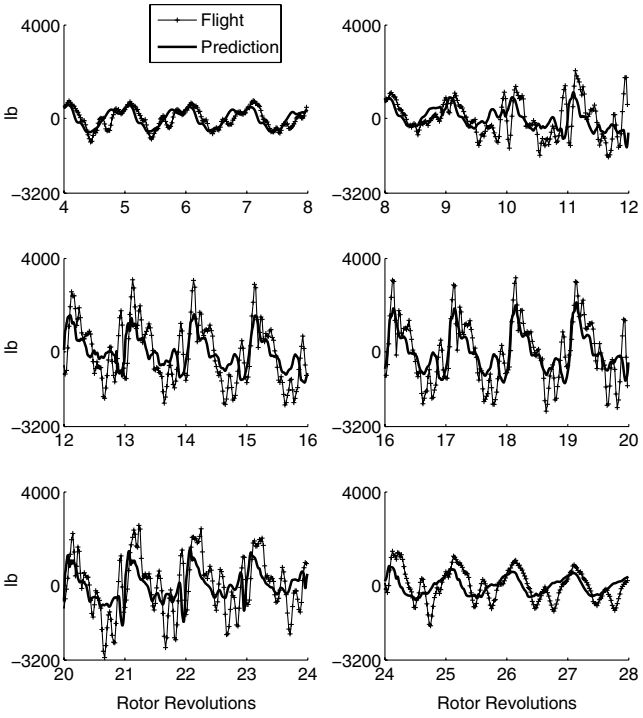

Fig. 24 Measured and predicted pitch-link load. (Predictions made using dynamic stall model, and mean removed.)

Figure 17 shows the sectional normal forces at 86.5%R, predicted by the coupled analysis. The prediction is able to show the basic features (mean and peak-to-peak) of the stall airloads during the course of the maneuver; however, the predicted high-frequency stall loads are less satisfactory. This might be due to the fact that many of these high-frequency stall events (four and five revolutions) have a very short life span and are difficult to predict. Figure 18 shows the sectional chord forces at the same radial station. Similar to a normal force, the stall spikes are not present in the predicted chord forces. The lower frequencies are well predicted for normal forces; due to this, the peak-to-peak loads are close to the test results. The lower frequencies are overpredicted for chord forces, leading to higher peak loads.

The quarter-chord pitching moments are shown at two radial stations, 77.5 and 86.5%R, in Figs. 19 and 20, respectively. Because the maneuver starts from a high-speed flight condition, the pitching moment for the first four revolutions is very similar to that of flight 8534. But, as we get further into the maneuver (between revolutions 10 and 20), the test data show three pitching moment stall cycles in each revolution. Two distinct stall cycles on the retreating side can be observed in the test data after the ninth revolution. An additional stall cycle appears on the advancing side between revolutions 12 and 20. This occurs under transonic flow conditions. The predicted pitching moments are plotted after removing the steady values. It is observed from Fig. 19 that the analysis is able to predict two distinct stall cycles on the retreating side during the course of the maneuver. The stall on the advancing side, which is a transonic stall, is not predicted by the analysis. The predicted stall spikes are not as sharp as the test data and weaken toward the tip. For example, the predicted pitching moments at 86.5%R, as shown in Fig. 20, are worse than the predictions at 77.5%R.

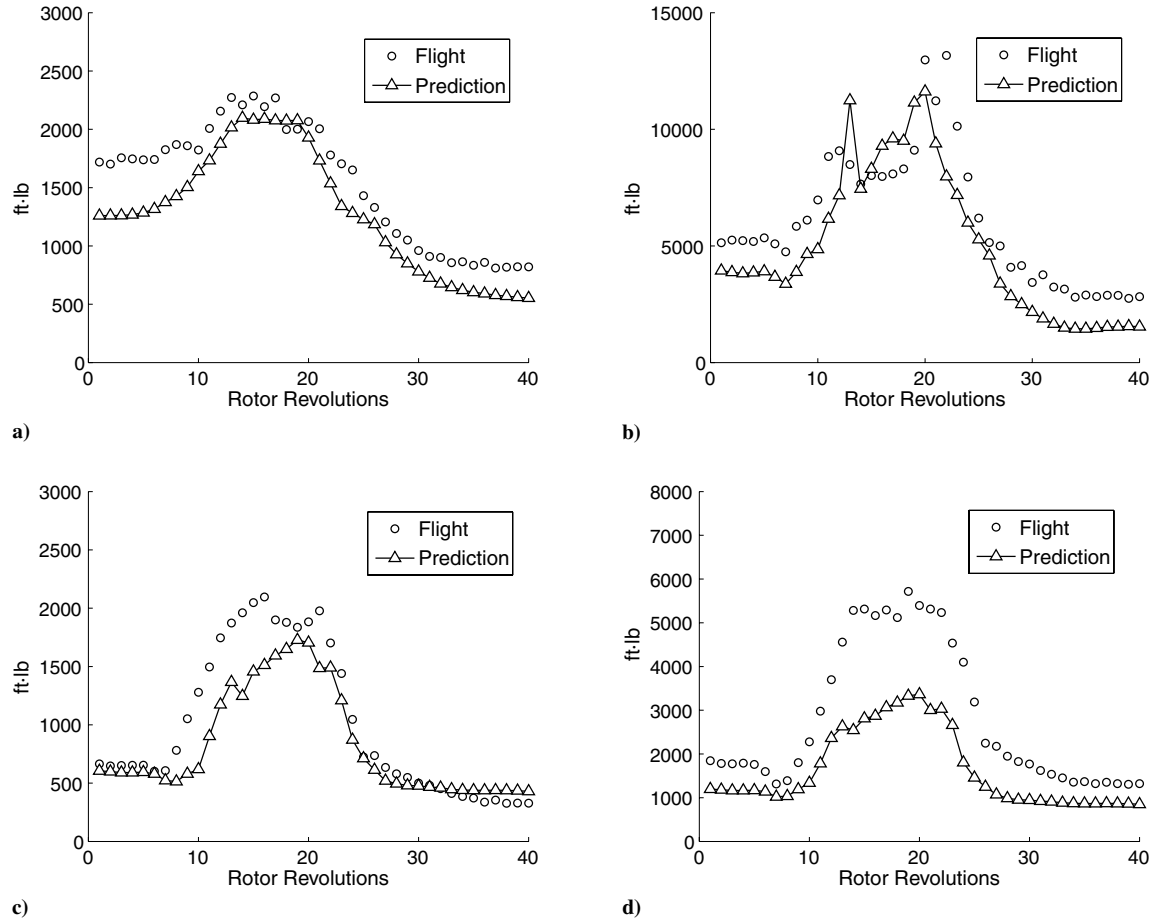

Fig. 25 Measured and predicted peak-to-peak structural loads: a) flap bending moment at 50%R, b) lag bending moment at 50%R, c) torsion moment at 30%R, and d) pitch-link load. (Predictions made using full aerodynamic model with free wake and dynamic stall.)

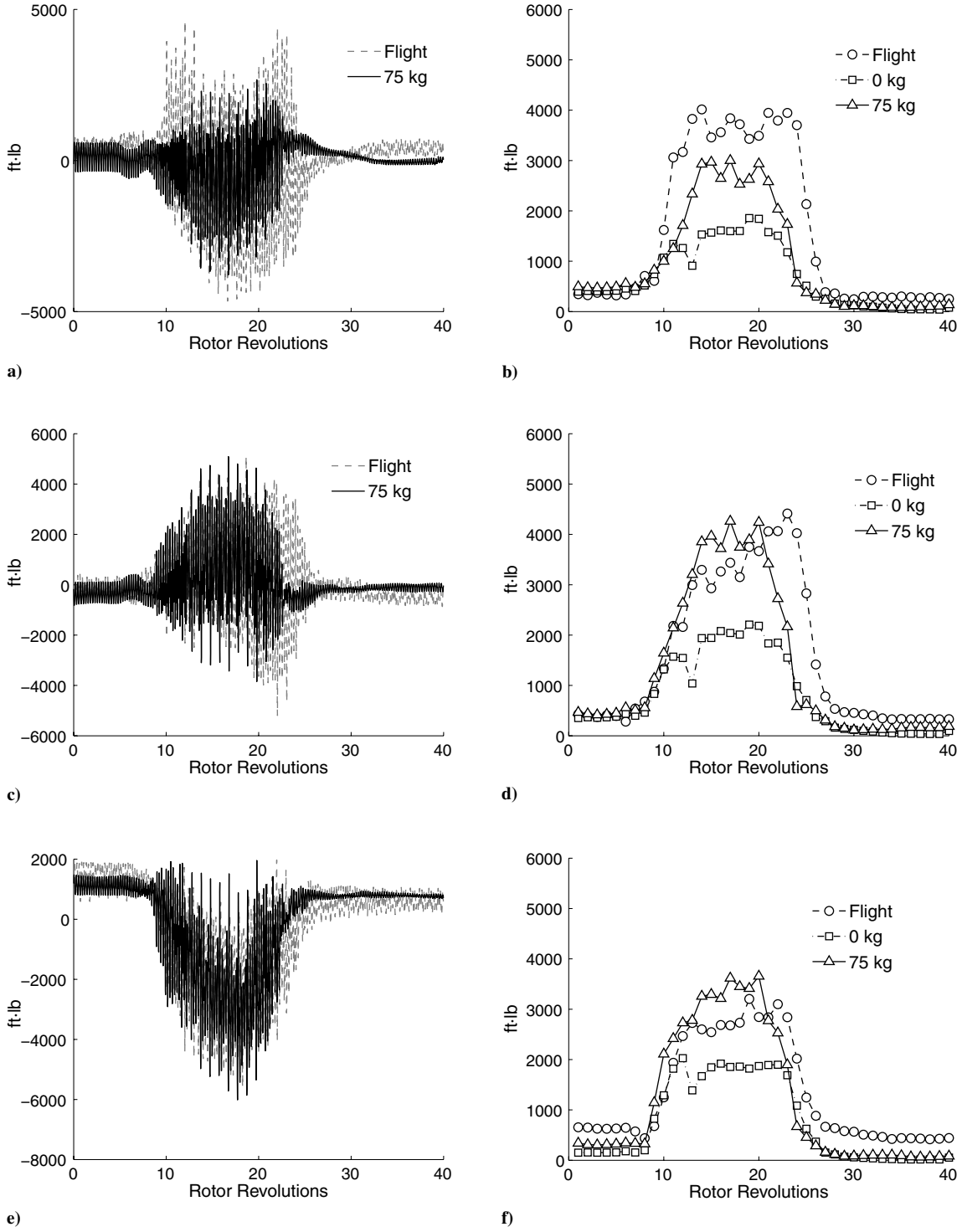

Fig. 26 Measured and predicted servo loads (mean removed): a) forward servo link load, b) half peak-to-peak forward servo link load, c) lateral servo link load, d) half peak-to-peak lateral servo link load, e) aft servo link load, and f) half peak-to-peak servo link load. [Predictions made using dynamic stall model with swashplate masses of 0 and 75 kg. Forward link (servo) located at 123°56′ azimuth, lateral link at 213°56′, and aft link at 303°56′ azimuth.]

Blade Structural Loads

The predicted flap bending moment at 50%R is shown in Fig. 21. The peak-to-peak moments are underpredicted by approximately 30% at the beginning of the maneuver, but the trends along the maneuver are similar to that of the test data. Figure 22 shows the lag bending moment at 50%R. Consistent with chord force predictions, the trends are less satisfactory when compared with the flap bending moments.

Figure 23 shows the predicted torsion moments at 30%R. The torsion moment is critical for an accurate prediction of the pitch-link load, which in turn drives the servo loads in a fixed frame. Accurate prediction of the torsion moment is a challenge due to the complicated nature of the pitching moment for this particular flight. The pitch-link load shows trends similar to the torsion moment (see Fig. 24). The peak-to-peak loads have been summarized in Fig. 25, and the torsion moment is overprotected during the steady part of the maneuver (see Fig. 25c).

Swashplate Servo Loads

To study the effect of swashplate dynamics, the baseline analysis was carried out with swashplate mass equal to zero; this amounts to

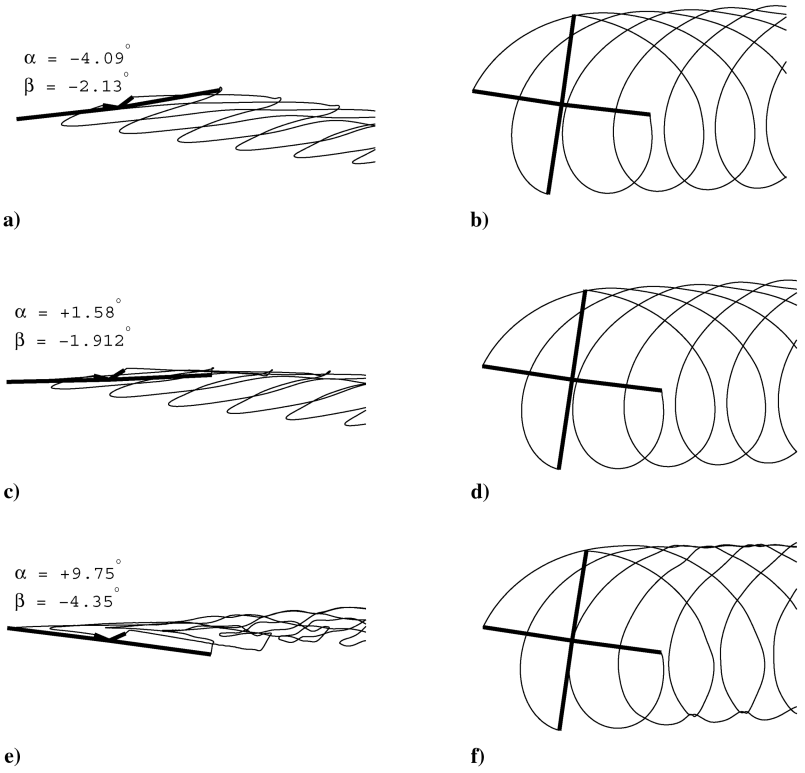

Fig. 27 Instantaneous rotor wake geometries during the maneuver: a) side view and b) top view at the end of revolution 6, c) side view and d) top view at the end of revolution 10, and e) side view and f) top view at the end of revolution 14. Using two wake turns, α is aircraft AOA, and β is aircraft sideslip angle.

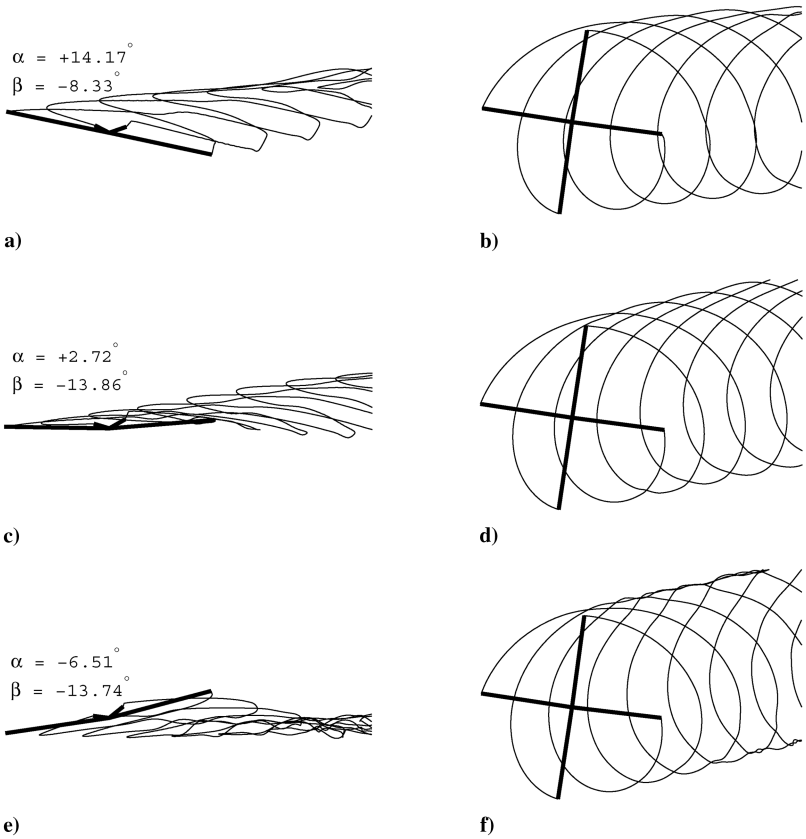

Fig. 28 Instantaneous rotor wake geometries during the maneuver: a) side view and b) top view at the end of revolution 18, c) side view and d) top view at the end of revolution 24, and e) side view and f) top view at the end of revolution 28. Using two wake turns, α is aircraft AOA, β is aircraft sideslip angle.

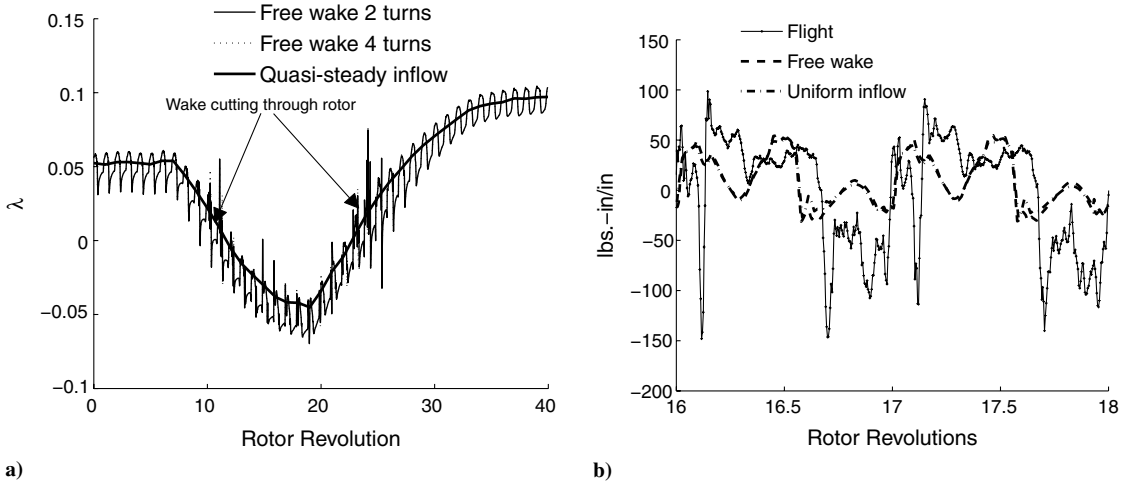

Fig. 29 Predicted inflow and effect of free-wake model on predicted pitching moment: a) predicted inflow at 86.5%R and b) pitching moment at 77.5%R. (Prediction made using static stall model.)

evaluation of servo loads through static force balance between the pitch link and the servos. The half peak-to-peak values are compared with the test data in Fig. 26. There is a significant improvement in peak-to-peak servo loads with swashplate dynamics, corresponding to a swashplate mass of 75 kg. However, no feedback effect on the blade loads is observed, as discussed later.

Fundamental Understanding

One of the primary objectives of the present study is to separate out the effects of wake and dynamic stall on the maneuver loads prediction. To accomplish this, the following three cases are considered: 1) uniform inflow and quasi-steady airloads using static airfoil properties, 2) free-wake and quasi-steady airloads, and 3) free wake and dynamic stall. The last case is was the baseline case. In addition, because the control angles are prescribed from the test data, a trim angle sensitivity study is carried out by perturbing the control angles by 10% of their baseline values.

Effect of Free-Wake Model

The rotor wake cuts through the rotor disk on two occasions. The side and top views of the wake geometry at different stages of the maneuver are shown in Figs. 27 and 28. At the end of revolution 6, the advance ratio μ is 0.358, and the aircraft angle of attack (AOA) α is -4.09 deg (+ve nose up), and the rotor wake is blown straight downstream (see Figs. 27a and 27b). As the aircraft angle approaches toward 0 deg, the wake gets closer to the rotor disk (see Fig. 27c), the sideslip angle is very small, and hence the rotor wake is fairly

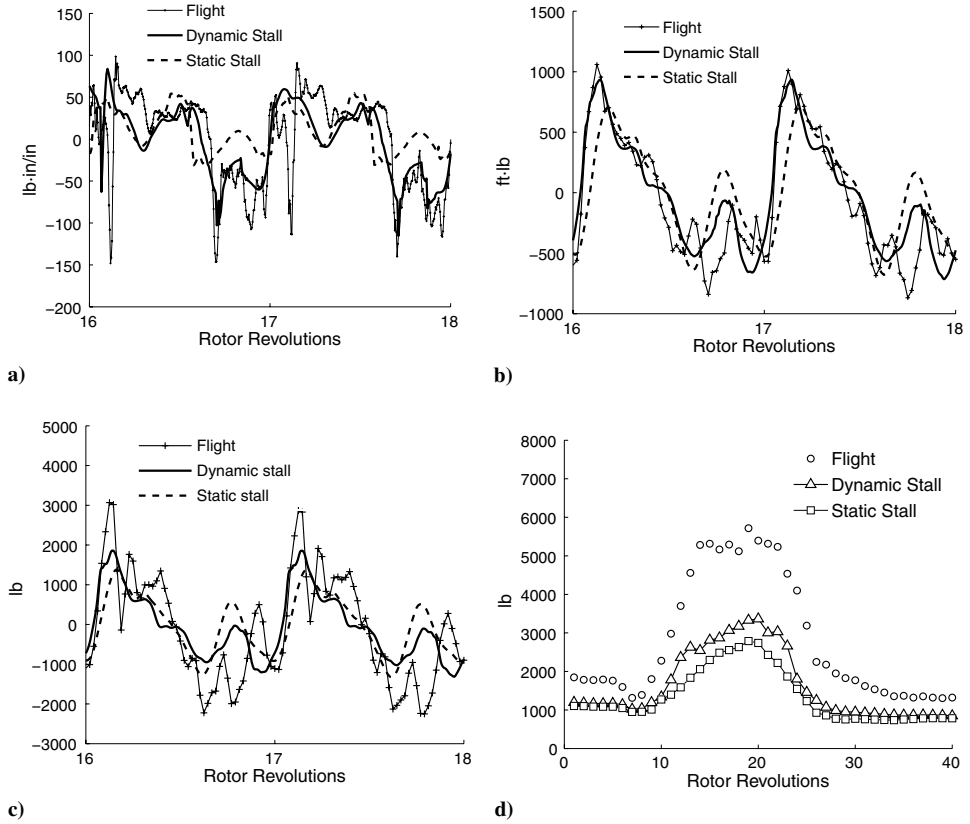

Fig. 30 Comparison of predicted blade loads using dynamic stall and static stall aerodynamic models: a) pitching moment at 77.5%R, b) torsion moment at 30%R, c) pitch-link load, and d) peak-to-peak pitch-link load.

straight, as seen in the top view (Fig. 27d). As observed in Figs. 27e and 27f, the rotor wake is above the rotor disk and is moving to the starboard side by the end of revolution 14 ($\alpha = +9.75$ deg and $\beta = -4.35$ deg). At this point, the helicopter is pulling a load factor of 2.08 g. The load factor is maintained above 2 g, between revolutions 14–18, after which the load factor starts to decrease. During this period, the wake remains above the rotor plane for most of time (see Fig. 28a). The rotor wake is again seen (Fig. 28c) in the disk plane at the end of revolution 24 ($\alpha = +2.72$ deg), when the wake starts to cut from top to bottom toward the end of revolution 24. By revolution 28, the rotor wake has descended below the rotor, as shown in Fig. 28e ($\alpha = -6.51$ deg and $\beta = -13.74$ deg).

The inflow predicted using the free-wake model is compared consistently with the uniform inflow calculated using the flight-test thrust and the effective shaft angle, with respect to the oncoming flow in Fig. 29a. The wake passage is clearly visible near revolutions 10 and 24. A choice of two or four free turns for the wake does not impact the inflow calculation, as there is no wake bundling phenomena near the disk. This is expected at relatively high speeds, as the rotor wake gets quickly blown away. However, the wake passage has no effect on the airloads (see Fig. 29b). It is shown later that the sectional angles of attack already operate under deep stall during these revolutions, and the wake-induced angle-of-attack variation has little effect on the airloads. The airloads are determined entirely by the poststall airfoil property tables. It is observed from the present analysis that, in general, the free wake does not affect any of the predicted airloads and structural loads.

Effect of Dynamic Stall

The pull-up maneuver is characterized by three stall cycles: one on the advancing side and two on the retreating side. The capability of

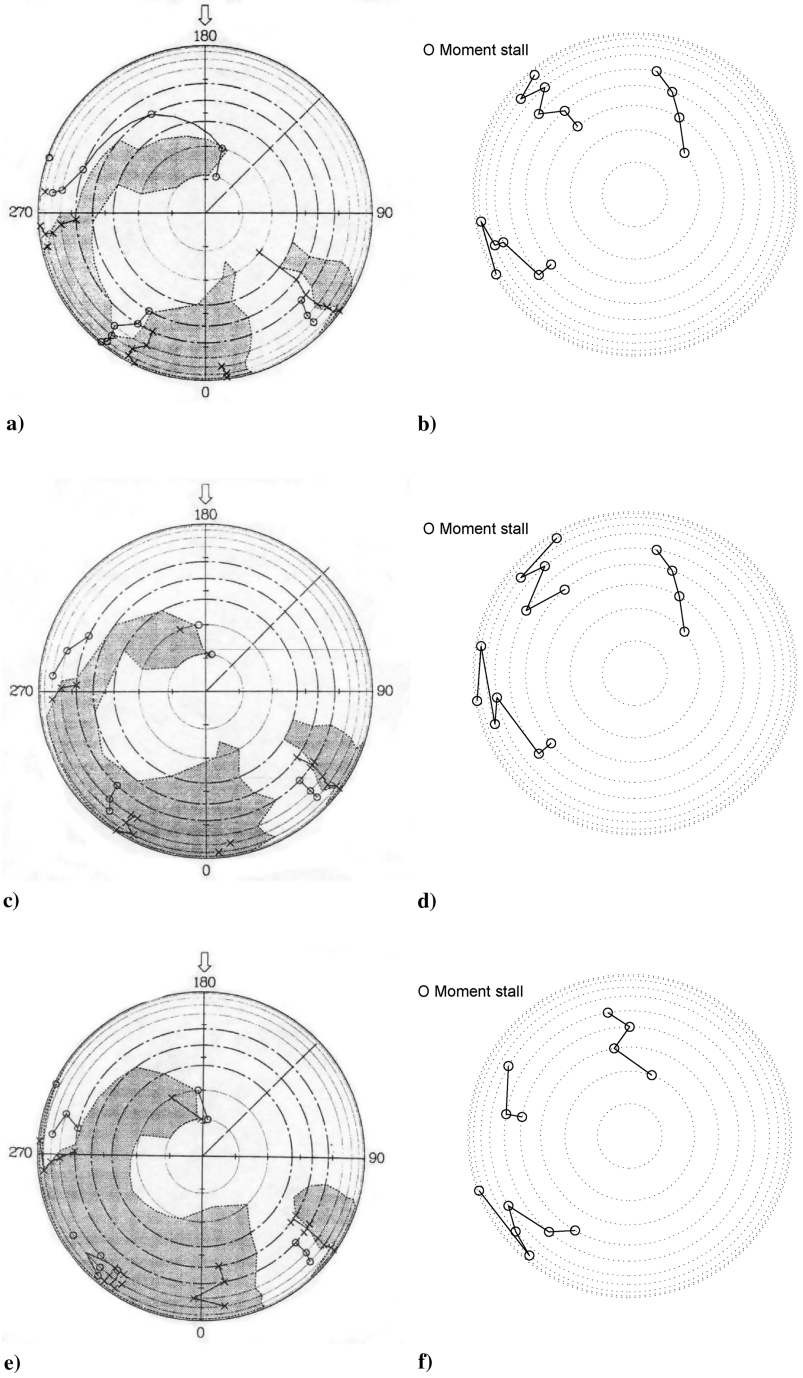

Fig. 31 Measured and predicted rotor stall maps. Flight stall maps for revolutions a) 14, c) 16, and e) 18, and predicted stall maps for revolutions b) 14, d) 16, and f) 18. (Predictions made using dynamic stall model and flight-test data from [4].)

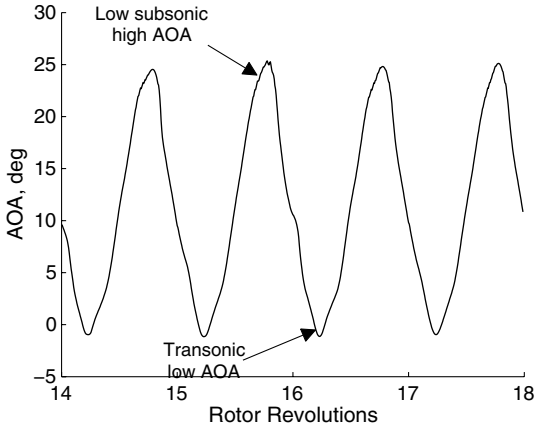

Fig. 32 Predicted AOA at 77.5%*R*. (Predictions made using dynamic stall model.)

lifting-line models is now examined in predicting these stall cycles. Figure 30a shows the predicted and measured pitching moment at 77.5%*R*, which highlights the importance of dynamic stall modeling. Both the waveform and magnitude of prediction require the dynamic stall model. The peak-to-peak pitching moment prediction is improved by more than 50% during revolutions 16–20.

However, the effect on the structural loads is less dramatic. The predicted peak-to-peak torsional moment at 30%*R*, using the dynamic stall model, shows improvement by 10 to 20%, with respect to those obtained without it (see Fig. 30b) during revolution numbers 16–20. Similar trends are exhibited by the pitch-link load (see Figs. 30c and 30d). It can be observed that the use of the dynamic stall model caused a significant impact on the peak-to-peak loads during the high-load factor regime (e.g., during revolution 14, when the load factor is more than 2.0 g, an improvement of 24% is observed for peak-to-peak pitch-link load, and for revolution 15, the gain is 23%). The gain in structural loads is less significant, because the peak-to-peak loads are determined primarily by one revolution, whereas the stall loads are mostly four and five revolutions.

The rotor stall maps showing moment stalls for revolutions 14, 16, and 18 are shown alongside stall maps from the flight test in Fig. 31. The flight-test stall maps reveal three stall cycles in the outboard region of the rotor disk: a stall on the advancing side near 50 deg azimuth followed by two stall cycles on the retreating side. The predicted stall maps also show three moment stall cycles. The first stall, occurring near the 180 deg blade azimuth, is starting from the blade inboard stations (55%*R*). The other two moment stalls are occurring in the retreating side, similar to the flight test. To understand the mechanism of these stalls, we need to look at the AOA at the onset of moment stall. Figure 32 shows the angle-of-attack variation at 77.5%*R*. The operating envelope (see Fig. 33a) for the SC1095 R8 airfoil at 77.5%*R* at revolution 16 reveals that when the blade reaches the 180 deg azimuth and attains an AOA of 10 deg, the local Mach number of 0.54 is sufficient to take the blade over the static stall limits, which triggers the dynamic stall model, and thus the first stall cycle is predicted near 180 deg. The remaining two stall cycles occur in a similar manner, with the AOA remaining deep inside the static stall region. The contribution of the leading-edge vortex to the quarter-chord pitching moment from the three stall events for revolutions 14–18 is shown in Fig. 33b. It appears that the contribution is not large when enough compared with the measurements. This underprediction leads to a reduced nose-down torsion deformation, which in turn causes the first stall to occur earlier in the azimuth. Figures 33c and 33d show the airfoil operating envelopes at 86.5 and 77.5%*R*, respectively, using all three aerodynamic analyses. It shows that all analyses predict the blade to be operating under a deep stall condition. This is the reason inflow variation has little or no effect on the loads prediction using the present analysis.

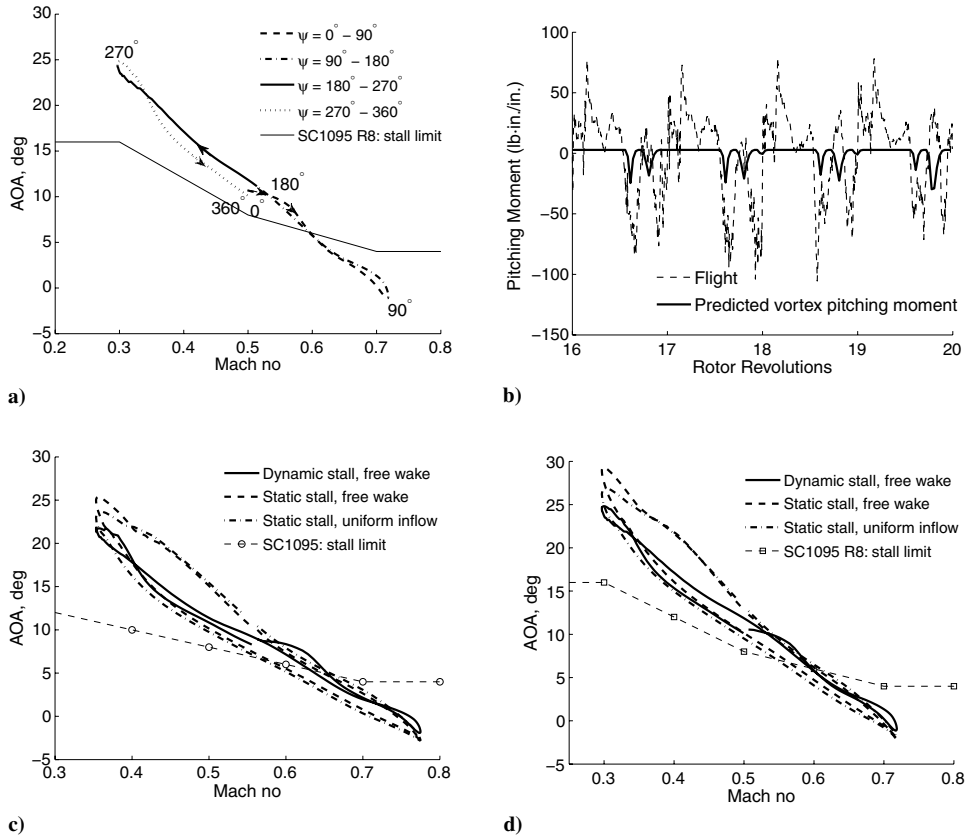

Fig. 33 Leading-edge vortex contribution to quarter-chord pitching moment at 77.5%*R* and predicted airfoil operating envelopes during revolution 17: a) AOA at 77.5%*R*, b) vortex-induced quarter-cord pitching moment, c) AOA at 86.5%*R*, and d) AOA at 77.5%*R* (all analysis).

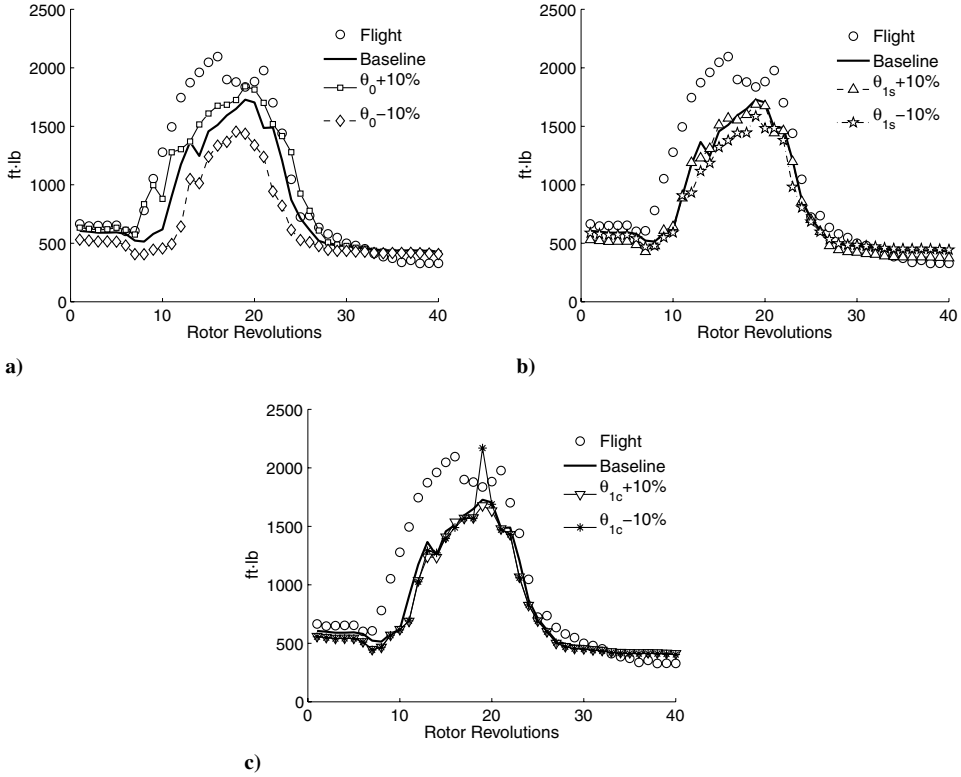

Fig. 34 Effect of initial trim angle on the predicted torsion moment at 30%R: a) collective perturbation, b) longitudinal cyclic perturbation, and c) lateral cyclic perturbation. (Predictions made using dynamic stall model.)

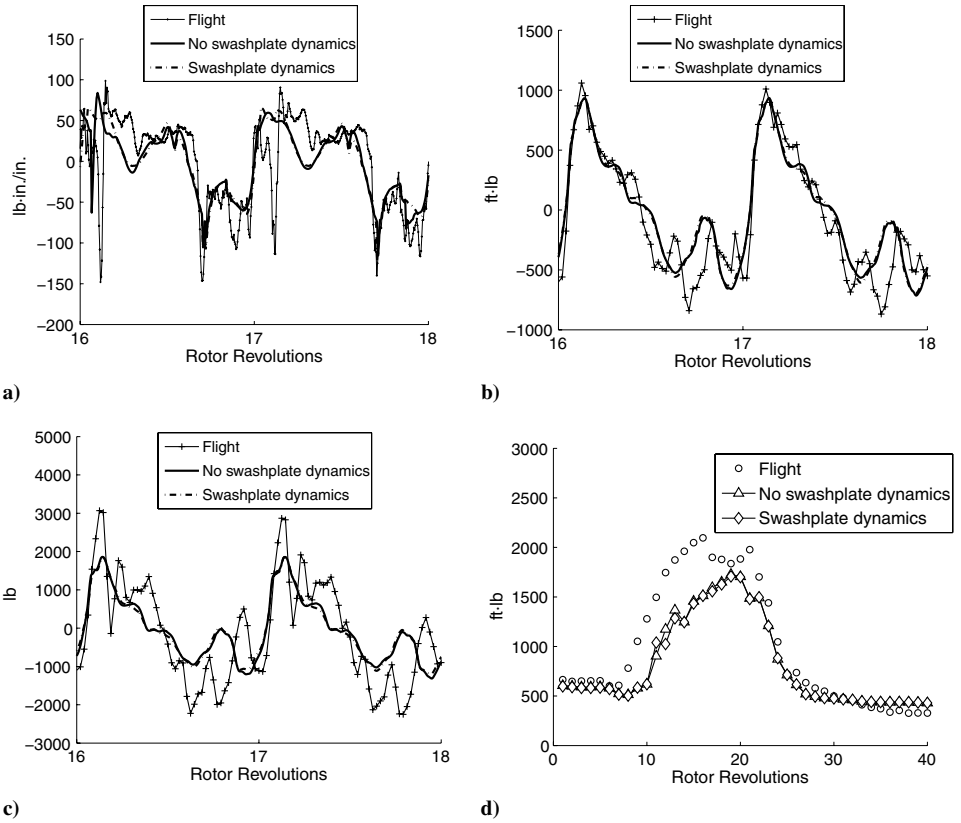

Fig. 35 Effect of swashplate dynamics on blade loads: a) pitching moment at 77.5%R, b) torsion moment at 30%R, c) pitch-load link, and d) peak-to-peak torsion moment at 30%R. (Predictions made using dynamic stall model and swashplate mass of 75 kg.)

Sensitivity to Control Pitch Angles

Because the present flight condition is a prescribed maneuver, and because it is initiated from trim angles calculated for steady flight conditions, it is important to understand the sensitivity of the analysis to the pitch control angles. The effect of perturbing the collective and lateral cyclic angles, by 10% of the baseline value, on the predicted peak-to-peak torsion moment at 30%R is shown in Fig. 34. A variation in the collective angle seems to have the most significant impact on the overall dynamics of the rotor, as depicted by the predicted peak-to-peak torsion moment. Increasing the collective angle by 10% causes an increase in the predicted torsion moment from the baseline (see Fig. 34a), whereas a reduction by 10% results in significant underprediction. This is due to the sensitivity of the predicted pitching moment to the AOA, which is primarily governed by the control angles. This calls for the need of better estimation of the control angles and use of a flight dynamics module with the capability to predict the dynamics of the helicopter. The longitudinal, and latter, cyclic perturbation does not have a significant effect on the overall dynamics, as shown in Figs. 34b and 34c.

Effect of Swashplate Dynamics

A swashplate mass of 75 kg (165 lb), based on a previous study [14], is used to study the effect of swashplate dynamics on rotor and servo loads. The predicted servo loads waveform and peak-to-peak values are shown in Fig. 26, and the peak-to-peak values show fair correlation with the test data. Figure 35 shows the predicted pitching moment at 77.5%R, the torsion moment at 30%R, and the pitch-link load. The swashplate dynamics do not seem to affect the rotor loads. But the swashplate dynamics do have a strong influence on the servo loads, which are predominantly four and eight revolutions (20% of four revolutions). Figure 36 shows the predicted trends for the servo loads for revolutions 4 and 8. It can be observed that, in the absence of any swashplate dynamics (swashplate mass of 0 kg), the predicted servo loads are dominated by four revolutions, and these four revolutions in the fixed frame come from the three-, four-, and five-revolution pitch-link loads in a rotating frame. It should be noted that, even though the peak-to-peak pitch-link load is underpredicted, the swashplate loads show better correlation with the flight test, because the analysis is able to predict the three-revolution pitch-link load

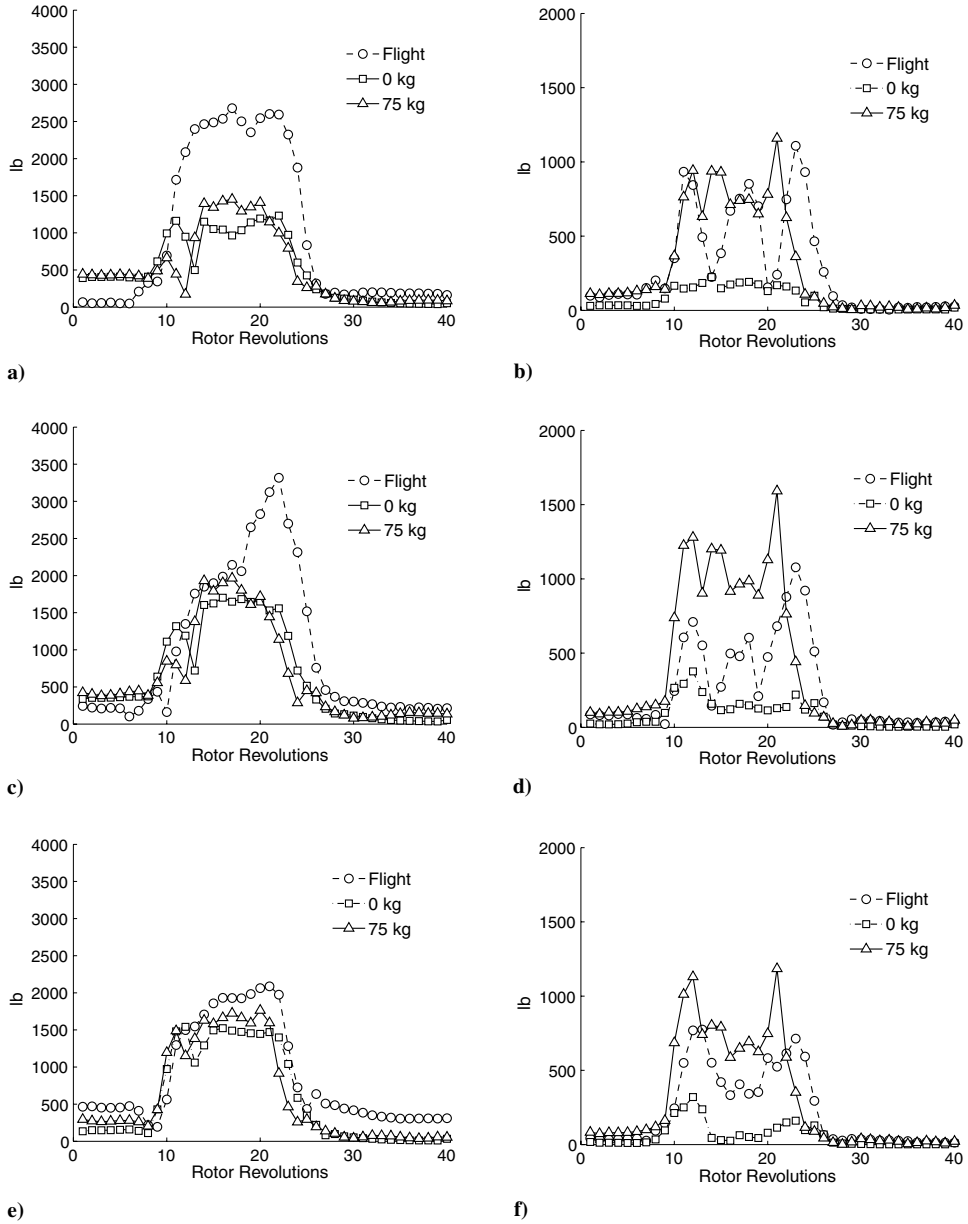

Fig. 36 Measured and predicted four- and eight-revolution servo loads. Forward link at a) four and b) eight revolutions, lateral link at c) four and d) eight revolutions, and aft link at e) four and f) eight revolutions. (Predictions made using dynamic stall model.)

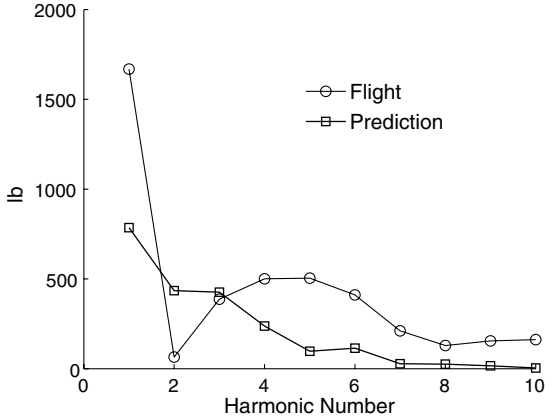

Fig. 37 Measured and predicted pitch-link load harmonics for revolution 15. (Swashplate dynamics not included.)

accurately, as shown in Fig. 37. Furthermore, when the swashplate mass is included in the analysis, the four-revolution prediction improves by 20–40%, but the eight-revolution servo loads, which are underpredicted in the absence of the swashplate dynamics, are now overpredicted. The overprediction occurs because the swashplate fundamental frequency for a mass of 75 kg lies close to revolution 8 (9.48 revolutions).

Conclusions

The airloads, the blade loads, the pitch-link loads, and the swashplate servo loads of the UH-60A helicopter were predicted and analyzed in a high-g pull-up maneuver. The rotor control angles and the flight dynamic parameters (flight path and velocities, attitude angles and rates) were prescribed from flight-test measurements (counter 11029 of the UH-60A Airloads Program). A multibody finite-element structural model, including a swashplate servo model, was coupled in time with an unsteady lifting-line aerodynamic model. The coupling in time was a straightforward time-marching procedure (tight coupling in rotorcraft nomenclature) without any subiterations. The key objective of this paper was to study the effects of structural dynamics, free wake, dynamic stall, and rotor control angles separately on the loads mechanism of the maneuver. The purpose of using the lifting-line aerodynamic model was to isolate the effects of free-wake and dynamic stall modeling. The accuracy of the structural model was first studied in isolation by calculating the blade loads, using the measured airloads, the damper forces, and the control angles over the entire 40 revolutions of the maneuver. The coupled analysis was then used to examine the accuracy level of the lifting-line aerodynamic model in predicting the structural loads. Because the maneuver was prescribed and not simulated from the first principles, the sensitivity of the predicted loads to the prescribed control angles were also studied. Based on this study, the following key conclusions were drawn:

1) The pull-up maneuver appeared almost entirely to be a stall-dominated maneuver. The dynamic stall model, not the free wake, provided the most significant improvement to predicted rotor loads. Almost up to 75% of a typical airfoil operating envelope (outboard of 67.5%R) during the 10–25 revolutions occurred beyond the static stall boundary. Thus, the sectional airload properties were governed predominantly by stall phenomenon.

2) Similar to the flight test, for which three distinct stall regions were reported, the analysis also predicted three stall cycles. However, only the two retreating blade cycles were predicted near the correct regions of the rotor disk. The advancing blade transonic stall cycle was not predicted at all. Instead, the third cycle was predicted on the retreating side, together with the first two. In the analysis, all of the cycles occurred due to the multiple leading-edge vortex shedding phenomena, governed entirely by the semiempirical time constants.

3) The rotor wake passed through the rotor disk during, approximately, revolutions 10 and 24. The present analysis does not predict any significant perturbation in the airfoil operating envelopes due to the wake during these revolutions. In general, between the uniform inflow and the free wake, there was 2–4 deg perturbation in the sectional angles of attack. However, they occurred in the stalled regions with minor impact on the sectional airloads.

4) The predicted peak-to-peak structural loads were unsatisfactory in general. During the peak load factor of the maneuver, 10–22 revolutions (above 1.75 g), the flap bending moments were closest to the test data (10–20% underprediction), followed by chord bending (25% overprediction), then torsion moment (30% underprediction), and finally the pitch-link load (50% underprediction). In addition, some of the key loads showed inconsistent trends. For example, the flap bending moment in the initial part of the maneuver, which was a steady level flight, was underpredicted by 30%, whereas the torsion moment was overpredicted by 30%.

5) The peak flap bending error was consistent with the measured airloads and showed the same level of error as the lifting-line airloads. The chord bending error was primarily due to the absence of the nonlinear damper force in the coupled analysis. In the case of the measured airloads, including damper force, the predictions were similar to the flight-test values. The error in the torsion moment and the pitch-link load stemmed entirely from the error in the stall airloads. With the measured airloads, both showed the correct trends.

6) The swashplate servo loads were determined by the three-, four-, and five-revolution pitch-link loads and the dynamics of the swashplate. The latter appeared to be an important contributor during the maneuver (unlike the case of level flight). However, the servo loads during the maneuver were dominated primarily by four-revolution loading, similar to the level flight. Their peak magnitudes were, however, magnified three (forward link) to five times (aft link) when compared with level flight. The analysis predicted this trend correctly, primarily due to the accuracy of the three-revolution pitch-link load prediction. The analysis also showed the significant impact of swashplate dynamics on the eight-revolution loads.

Acknowledgment

The authors acknowledge the support provided by the NASA Research Announcement, with G. P. Guruswamy as the technical monitor.

References

[1] Datta, A., Nixon, M., and Chopra, I., "Review of Rotor Loads Prediction with the Emergence of Rotorcraft CFD," *Journal of the American Helicopter Society*, Vol. 52, No. 4, Oct. 2007, pp. 287–317. doi:10.4050/JAHS.52.287

[2] Kufeld, R. M., Balough, D. L., Cross, J. L., Studebaker, K. F., Jennison, C. D., and Bousman, W. G., "Flight Testing of the UH-60A Airloads Aircraft," *American Helicopter Society 50th Annual Forum Proceedings*, AHS International, Alexandria, VA, May 1994, pp. 557–577.

[3] Bousman, W. G., and Kufeld, R. M., "UH-60A Airloads Catalog," NASA TM-2005-212827/AFDD TR-05-003, Aug. 2005.

[4] Bousman, W. G., "A Qualitative Examination of Dynamic Stall from Flight Test Data," *Journal of the American Helicopter Society*, Vol. 43, No. 4, Oct. 1998, pp. 279–295. doi:10.4050/JAHS.43.279

[5] Kufeld, R. M., "High Load Conditions Measured on a UH-60A in Maneuvering Flight," *Journal of the American Helicopter Society*, Vol. 43, No. 3, July 1998, pp. 202–211. doi:10.4050/JAHS.43.202

[6] Washuta, K. W., and Stocker, B. P., "Air-to-Air Combat Test (AACT 2) Maneuvering Flight Loads for UH-60A and AUH-76 Helicopters," U.S. Army Aviation Systems Command TR 86-D-1, April 1986.

[7] Bhagwat, M. J., Ormiston, R. A., Saberi, H. A., and Xin, H., "Application of CFD/CSD Coupling for Analysis of Rotorcraft Airloads and Blade Loads in Maneuvering Flight," *American Helicopter Society 63rd Annual Forum Proceedings* [CD-ROM], AHS International, Alexandria, VA, May 2007.

[8] Bhagwat, M. J., and Ormiston, R. A., "Examination of Rotor Aerodynamics in Steady and Maneuvering Flight Using CFD and Conventional Methods," *American Helicopter Society Specialists' Conference on Aeromechanics* [CD-ROM], AHS International, Alexandria, VA, Jan. 2008.

[9] Abhishek, A., Datta, A., and Chopra, I., "Comprehensive Analysis, Prediction, and Validation of UH-60A Blade Loads in Unsteady Maneuvering Flight," *American Helicopter Society 63rd Annual Forum Proceedings* [CD-ROM], AHS International, Alexandria, VA, 1–3 May 2007.

[10] Abhishek, A., Datta, A., and Chopra, I., "Comprehensive Analysis, Prediction, and Validation of UH-60A Blade Loads in Unsteady Maneuvering Flight," *Specialists' Conference on Aeromechanics* [CD-ROM], AHS International, Alexandria, VA, Jan. 2008.

[11] Yeo, H., "Investigation of Rotor Airloads and Structural Loads in Maneuvering Flight," *American Helicopter Society 64th Annual Forum Proceedings* [CD-ROM], AHS International, Alexandria, VA, 26 April–1 May 2008.

[12] Sitaraman, J., and Roget, B., "Prediction of Helicopter Maneuver Loads Using A Coupled CFD/CSD Analysis," *26th Congress of International Council of the Aeronautical Sciences* [CD-ROM], AIAA, Reston, VA, 14–19 Sept. 2008.

[13] Silbaugh, B., and Baeder, J. D., "Coupled CFD/CSD Analysis of a Maneuvering Rotor Using Staggered and Time-Accurate Coupling Schemes," *American Helicopter Society Specialists' Conference on Aeromechanics* [CD-ROM], AHS International, Alexandria, VA, 23–25 Jan. 2008.

[14] Abhishek, A., Datta, A., and Chopra, I., "Prediction of UH-60A Structural Loads Using Multibody Analysis and Swashplate Dynamics," *Journal of Aircraft*, Vol. 46, No. 2, 2009, pp. 474–490. doi:10.2514/1.35076

[15] Kufeld, R. M., and Johnson, W., "The Effects of Control System Stiffness Models on the Dynamic Stall Behavior of a Helicopter," *Journal of the American Helicopter Society*, Vol. 45, No. 4, 2000, pp. 263–269. doi:10.4050/JAHS.45.263

[16] Leishman, J. G., and Beddoes, T. S., "A Generalized Model for Unsteady Aerodynamic Behavior and Dynamic Stall Using Indicial Method," *Journal of the American Helicopter Society*, Vol. 36, 1990, pp. 14–24.

[17] Ananthan, S., and Leishman, J. G., "Predictions of Transient Rotor Wake Aerodynamics in Response to Time-Dependant Blade Pitch Inputs," *Journal of Aircraft*, Vol. 41, No. 5, 2004, pp. 1025–1041. doi:10.2514/1.3561

[18] Guruswamy, G. P., and Yang, T. Y., "Aeroelastic Time-Response Analysis of Thin Airfoils by Transonic Code LTRAN2," *Computers and Fluids*, Vol. 9, No. 4, 1981, pp. 409–425. doi:10.1016/0045-7930(81)90012-8

[19] Datta, A., and Chopra, I., "Validation of Structural and Aerodynamic Modeling Using UH-60A Airloads Program Data," *Journal of the American Helicopter Society*, Vol. 51, No. 1, Jan. 2006, pp. 43–58. doi:10.4050/1.3092877